

Final Draft
of the original manuscript:

Steglich, D.; Wafai, H.; Besson, J.:

Interaction between anisotropic plastic deformation and damage evolution in Al 2198 sheet metal

In: Engineering Fracture Mechanics (2010) Elsevier

DOI: 10.1016/j.engfracmech.2010.08.021

Interaction Between Anisotropic Plastic Deformation and Damage Evolution in Al 2198 Sheet Metal

D. Steglich^{a,c,1}, H. Wafai^a, J. Besson^b

^a GKSS Forschungszentrum Geesthacht, Institute of Materials Research, Materials Mechanics, Max-Planck-Str. 1, 21502 Geesthacht, Germany

^b Mines ParisTech, Centre des Matériaux, CNRS UMR 7633, BP87 91003 Evry Cedex, France

^c G.I.F.T., Pohang University of Science and Technology, Pohang, Gyeongbuk, 790-784, Korea

ABSTRACT – Deformation anisotropy of sheet aluminium alloy 2198 (Al-Cu-Li) has been investigated by means of mechanical testing of notched specimens and Kahn-type fracture specimens, loaded in the rolling direction (L) or in the transverse direction (T). Fracture mechanisms were investigated via scanning electron microscopy. Contributions to failure are identified as growth of initial voids accompanied by a significant nucleation of a second population of cavities and transgranular failure. A model based on the Gurson-Tvergaard-Needleman (GTN) approach of porous metal plasticity incorporating isotropic voids, direction-dependent void growth, void nucleation at a second population of inclusions and triaxiality-dependent void coalescence has been used to predict the mechanical response of test samples. The model parameters have been calibrated by means of 3D unit cell simulations, revealing the interaction between the plastic anisotropy of the matrix material and void growth. The model has been successfully used to describe and predict direction-dependent deformation behaviour, crack propagation and, in particular, toughness anisotropy.

Key Words: Anisotropy, Plasticity, Unit Cells, Void Growth, Ductile Damage, Kahn Specimen

¹ Corresponding author, dirk.steglich@gkss.de

1 INTRODUCTION

Aluminium alloys have been widely used since the early 1900s for structural engineering applications, in transportation industries and in civil engineering. New aluminium alloys have been further developed to satisfy the demands of transportation industries for high strength, improved damage resistance, as well as reduction of production cost. High strength, good corrosion properties and improved fracture toughness are some of the criteria to be met by newly developed alloys, which usually come with disadvantages such as higher weight or poor fatigue performance. Assessment of residual strength of aircraft structures has been a focus since the launch of NASA's ASIP (Airframe Structural Integrity Program) [1], and several authors have contributed to the development of models, methods and procedures to characterise and predict crack extension in aircraft aluminium alloys, e.g. [2-5]. Characterisation of alloys with respect to resistance against ductile crack extension has become an essential part of a damage-tolerance concept, which acknowledges the existence of cracks and structural damage. However, the R-curve approach of classical fracture mechanics and the respective standards are not suited to describe crack extension in thin sheets and shells, in particular because the deformation behaviour of rolled sheets is strongly anisotropic. Damage mechanics provides a unified approach combining the constitutive equations for anisotropic deformation with equations describing the degradation of the material, taking full advantage of the potential of the local approach [6, 7]. The use of damage mechanics is generally not restricted to assessment problems. This approach has become popular in metal forming and machining [8, 9].

Ductile damage is usually approached by using isotropic damage models, in which voids are assumed to be spherical while the matrix material is assumed to be isotropic. Assuming plastic isotropy of the matrix only, many authors have investigated the influence of the void geometry on the homogenised response of the material [10-12]. In these studies, the matrix has been treated by continuum plasticity, being homogenous and isotropic. For many materials, e.g. multiphase steels, composite materials and high-strength aluminium alloys this assumption cannot be used. Recently, an anisotropic plastic potential has been used to address delamination fracture in Al-Li-alloy under small scale yielding (SSY) conditions [13]. Apparently, there is a coupling between anisotropy and void growth due to the constraint added in the vicinity of the void. In order to account for this effect in a general way, a homogenisation procedure has to be carried out, which finally leads to a set of constitutive equations comprising a plastic potential, a flow rule, and an evolution equation for the porosity. For the sake of simplicity, porosity is commonly expressed as a scalar quantity; its evolution is therefore assumed to be isotropic. But evolution equations for non-isotropic voids require at least a non-scalar damage measure, e.g. for the modelling of ellipsoidal voids [14-16] or general anisotropic damage [17-19]. For orthotropic material like rolled sheets, various yield criteria are available, e. g. [20-23]. Anisotropy is expressed by using a structural tensor, which is based on the axes of orthotropy. In damage models this framework may be used together with the assumption that effects caused by matrix anisotropy and void shape are independent [24]. This is called 'weak coupling' of damage and anisotropy.

The material considered in the present study is a new member of the Al-Cu family, developed in view of applications in aerospace industry (2xxx series). These alloys are specifically designed to have good mechanical properties in order to use them for structural components in aircrafts. They have copper (Cu) as the major alloying element and hardening is achieved by aging. The new alloy Al 2198 contains also lithium as an alloying element to reduce the density and increase Young's modulus and thus to save weight. The marriage of Li to Al offers the promise of substantially reducing the weight of aerospace alloys, since each 1 wt. % Li added to Al reduces density by 3% and increases the elastic modulus by about 6%. It has been solution heat treated, cold worked to improve strength, and artificially aged (T8 temper). It has superior yield strength to the well established alloy Al 2024, and it is claimed by the producer to have improved damage tolerance, higher corrosion and fatigue resistance, and thermal stability. If true, this would make the alloy ideal for aircraft fuselage skin and other similar applications [25]. Actual research aims on the optimisation of its damage tolerance, which is of particular relevance for commercial (civil) aircrafts.

This paper studies orientation-dependent deformation under static loading conditions, failure and damage mechanisms, and their prediction by numerical models. Fractography clarifies the basic mechanisms of failure, which will be modelled using a damage model combined with a description of anisotropic plastic deformation. This material model was realised in the framework of finite elements. The respective parameters are calibrated from simulations of voided representative volume elements (RVEs), which are assumed to be typical for the microstructure. Special emphasis is laid on the interaction between material anisotropy and void growth. Mechanical tests of U-notched tensile specimens machined for different orientations of the sheet metal as well as Kahn fracture mechanics specimens provide additional information on damage and fracture mechanisms. The constitutive model is finally applied to simulate the experimental tests.

2 CONSTITUTIVE BEHAVIOUR: ANISOTROPY AND DAMAGE

The main focus of the present investigation is on the interaction of plastic anisotropy and void growth and coalescence. The material selected for validation is a commercial aluminium alloy, for which non-quadratic yield criteria are recommended. In a previous investigation [26], it was proven that the Bron model [27] based on an anisotropic yield surface is able to predict the direction-dependent deformation response of different types of flat specimens machined from rolled sheets. This particular constitutive model (a detailed description of the model is given in the Appendix) has been extended in order to incorporate the effect of hydrostatic pressure on the growth of micro-voids. This was done by replacing the equivalent stress in the yield function of a voided aggregate, Eq. (A16), by the respective definition of the anisotropic deformation model, Eq. (A12). A similar approach has been proposed by Bron and Besson [28] based on the Rousselier model [29]. Hardening and damage evolution are assumed to be isotropic, expressed by the plastic equivalent strain, p , and the void volume fraction, f .

The mathematical model was realised in the object-oriented FE code Zébulon [30]. It has been linked via the material library Z-Mat to the commercial finite element program ABAQUS/Standard, which was used to perform the simulations in the present contribution.

The model parameters were identified sequentially. The strain hardening function in terms of true stress and true (logarithmic) plastic strain was taken from a tensile test in L-direction up to the load maximum and extrapolated using a power-law function

$$\sigma = 468 \text{ [MPa]} (1 + 40.95 p)^{0.1202}. \quad (1)$$

The elastic constants were set to be $E=73000$ MPa and $\nu=0.33$. Assuming that the effect of damage on yielding is negligible, the values for the shape parameters of the yield surface a , b_1 , b_2 and α as well as the parameters describing the orthotropy c_i^k were calibrated based on force-elongation and reduction of width signal taken from smooth and notched samples. Details of the identification procedure can be found in [26]. Table 1 summarises the values used for the material under investigation. It is worth mentioning that the ‘best’ tensile properties among the three tested orientations were obtained for L-orientation, leading to the highest yield strength and ultimate strength, see Table 2.

For the use of porosity-base damage models, an initial cavity fraction has to be defined. This was done by analysing different cross sections of the material and measuring the area fraction of visible particles. The material contains coarse intermetallic phases containing iron and silicon which act as damage initiation sites during straining of the material. As these phases are relatively brittle they tend to break or debond during the early stages of deformation. For that reason they are considered as initial porosities, f_0 . The material also contains secondary particles such as dispersoids and strengthening precipitates. Dispersoids may lead to void nucleation for high strain levels. Another damage mechanism in Al-Li alloys is grain boundary decohesion which is observed in the present case. In this work it is assumed that secondary nucleation only starts when a critical strain level is reached (ε_0). The nucleation rate (parameter A in Eq. (A19)) is then high, representing rapid material failure by both void nucleation on secondary particles and grain boundary decohesion.

Despite the fact that more rigorous approaches exist to model anisotropic damage evolution, an isotropic description of damage is chosen here. This is motivated by the material’s inclusion morphology, which appears isotropic rather than anisotropic. Moreover, the use of a rather simple isotropic model masks the inherent difficulties with finding appropriate evolution laws for different damage components or the restrictions to axisymmetric void shapes anticipating the use of those models in orthotropic sheet material.

3 CELL MODELS

In order to quantify the effect of porosity evolution, stress triaxiality, void shape, and void distribution on void growth and coalescence, unit cell approaches are commonly used [31-35].

Micromechanically motivated values for a critical porosity, corresponding to plastic collapse of a cell, can be derived by this means. The continuum is imagined as a periodic array of representative volume elements (RVEs), which are assumed to be statistically representative for the microstructure. Usually in the context of models describing isotropy, a hexagonal cylindrical unit cell containing a spherical void is considered. The hexagonal cylinder is then approximated by a circular cylinder allowing for axisymmetric calculations, and due to symmetry, only a quarter model has to be considered.

In the presence of deformation anisotropy, however, these simplifications are not justified. Mesoscopic deformation and void growth then depend on the main loading direction and are a function of the material anisotropy. To investigate this effect, 3D configurations have to be considered, similar to the approach presented by Yerra et al. [36] for voided single crystals using the framework of crystal plasticity. Here, the RVE calculations are used for two reasons: (i) to calibrate the model parameters of the damage model on the basis of the unit cell behaviour, (ii) to investigate the effect of the anisotropic deformation behaviour on void growth.

The configuration used in the present studies requires a primitive cubic arrangement of voids. It consists of a cube of initial edge lengths $2L_0$ containing a spherical void in its middle. This set-up was chosen from among other possible configurations (e.g. hexagonal or body centred cubic arrangements) because it provides a response close to the one of the frequently used approximation by hexagonal arrangements and axisymmetric cells [34]. While the choice of the arrangement plays a major role for large voids, i.e., high volume fractions, it might be negligible for small void volume fractions. In a microstructural analysis the nearest neighbour distance was evaluated for three orthogonal cross sections [37] of the material. It was found that there are no significant differences in particle's neighbour distances. However, a possible alignment of particles in lines in or perpendicular to the rolling direction is not reflected by the nearest neighbour distance. For the sake of simplicity, a homogenous arrangement of voids is assumed here. An anisotropic spacing could be realised by changing the aspect ratio of the unit cell accordingly, see [15].

The matrix around the void is assumed to deform elastic-plastically as a consequence of external tractions applied to the RVE's outer surfaces. The principal axes of the RVE are set to be collinear with the axes of orthotropy. The void's surface is assumed to be traction-free. While loading is applied in the directions of orthotropy, threefold symmetry can be exploited. Consequently, only 1/8 of the RVE has to be modelled. The void radius, R_0 , is determined by the void volume fraction, f_0 , and the RVE's dimension, L_0 :

$$R_0 = L_0 \sqrt[3]{\frac{6f_0}{\pi}} . \quad (2)$$

The initial void volume fraction was taken as 0.0027 [26] for the material under consideration. The principal axes of the cube coincide with the rolling direction (L), transverse (T) and short transverse (S) direction. Figure 1

shows a typical symmetric cell used here.

The cell is subjected to ‘mesoscopic’ true principal tractions, $\Sigma_1 \geq \Sigma_2 = \Sigma_3$, which are the average reaction forces at the cell boundaries per current areas. The ratio of surface tractions Σ_1 and Σ_2 are calculated from the stress triaxiality T

$$T = \frac{\Sigma_h}{\Sigma_e} = \frac{1}{3} \frac{\Sigma_1 + 2\Sigma_2}{\bar{\sigma}} \quad (3)$$

using the definition of the effective stress provided in (A12) and the model parameters given in Table 1. The respective ratios Σ_2/Σ_1 for monotonous loading are infinite ($T=0.33$, uniaxial tension), 0.1428 ($T=0.5$), 0.2940 ($T=0.75$), 0.3999 ($T=1$), 0.4782 ($T=1.25$), 0.5384 ($T=1.5$) and 0.6249 ($T=2$). Interestingly, these values differ only by 0.08 % from those which can be calculated using the von Mises effective stress instead of Eq. (A12)

In order to guarantee continuity, the boundaries of the cell are constrained to remain straight and orthogonal during deformation. The ‘mesoscopic’ principal strains, E_i ($i = 1, 2, 3$), are defined as a function of the displacements u_1 , u_2 and u_3 :

$$E_1 = \ln\left(1 + \frac{u_1}{L_0}\right); \quad E_2 = \ln\left(1 + \frac{u_2}{L_0}\right); \quad E_3 = \ln\left(1 + \frac{u_3}{L_0}\right), \quad (4)$$

A ‘mesoscopic’ effective strain can be defined as

$$E_e = \frac{\sqrt{2}}{3} \left[(E_1 - E_2)^2 + (E_1 - E_3)^2 + (E_2 - E_3)^2 \right]^{\frac{1}{2}}. \quad (5)$$

The Riks algorithm in the FE-program ABAQUS is used in order to prescribe a constant stress triaxiality during the loading process. The constitutive response of the matrix material is taken as elastic-plastic following the Bron model, with parameters described in the previous section.

For the FE-model, isoparametric linear 3D elements were used. To investigate the effect of material orientation, a local coordinate system specifying L-, T- and S- direction was used. By this means three different configuration are investigated: The main loading direction (x-axis) the L-direction, the T-direction, and the direction which has an angle of 45° from the L-direction, which is called the D-orientation. In case the main loading direction is the L- or T-direction, the symmetry of the problem was exploited. For the D-orientation in general, the symmetry conditions perpendicular to the S-direction cannot be used. Therefore a half model instead of an 1/8 model is required. However, test simulations revealed that the influence of symmetry conditions is negligible for the material parameters used here. Thus, for all configurations, a 1/8 model was used to make computations more efficient.

The mechanical response in terms of mesoscopic effective stress vs. effective strain of the cell is evaluated and compared for the stress triaxialities 0.33 (uniaxial tension), 0.5, 0.75, 1.0, 1.25,

1.5 and 2.0. Furthermore, the current void volume fraction was evaluated via the volume of all finite elements in the model and the outer dimensions of the RVE,

$$f = 1 - \frac{\sum_{i=1}^n V_i}{(L_0 + u_1)(L_0 + u_2)(L_0 + u_3)}. \quad (6)$$

This allows monitoring the void growth rate and specifying the 'critical' state of the cell defined as the beginning of strain localisation. The onset of void coalescence becomes apparent by the sudden drop of the effective stress, which is generally caused by an intervoid necking mechanism in the cell perpendicular to main loading direction. At this stage the void volume fraction starts to evolve strongly with increasing effective mesoscopic strain.

It should be mentioned here that the assumption that $\Sigma_1 \geq \Sigma = \Sigma_3$, made for the macroscopic loading of the cell, implies an axi-symmetric stress state. In this case, the triaxiality is determined by one ratio of principal stresses, Σ_2/Σ_1 . As the triaxiality alone generally cannot uniquely describe a stress field, multiple stress states with different principal stress ratios can result in the same stress triaxiality, and the macroscopic stress-strain response as well as the void growth and coalescence behaviour of the voided cell are different for each stress state, see e.g. [38, 39]. In order to characterise the effects of stress triaxiality on the macroscopic stress-strain behaviour of the unit cell and on void growth, a function of the principal stress ratios must be in the modelling. The aforementioned restriction with respect to stress states has been used here because, beside its simplicity, it provides a lower bound for the void growth behaviour and thus leads to conservative predictions of the void volume fraction at coalescence [39].

4 U-NOTCHED AND KAHN SPECIMENS

In order to investigate the mechanical deformation and fracture behaviour of the material, tests of U-notched and Kahn type specimens [40] were performed. U-notched specimens were used to study the deformation and damage behaviour at elevated triaxialities and to calibrate the damage parameters of the constitutive law. Kahn specimens were observed for the purpose of studying crack initiation and extension and to validate the material model. All specimens were machined from the same rolled sheet of thickness 3.1 mm. Tests were performed under displacement control using a servo hydraulic Zwick 1484 testing machine (maximum force 200 kN) with a constant cross head speed of 0.5 mm/min. Measured values were tensile force and notch opening displacement (NOD). The test results are presented as force vs. NOD curves.

4.1 U-notch tensile specimens

Two different kinds of specimens were used: specimens with notch radius of 1 mm and notch radius of 2 mm. The shape and dimensions of the tested specimens are given in [26]. Specimens were machined in three directions with respect to the rolling direction of the sheet:

- along the rolling direction, L 'Longitudinal', three specimens each radius,
- perpendicular to the rolling direction, T 'Transversal', three specimens each radius,
- 45° to the rolling direction, D 'Diagonal', three specimens each radius.

Despite the fact that the specimen thickness is comparably small, 3D discretisation has to be used for the simulations to properly capture the void evolution [41]. Quadratic elements with reduced integration (3D bricks with 20 nodes) were used. The threefold geometrical symmetry of the specimens was exploited, thus one eighth of the specimen was modelled.

A coarse mesh was used for the model except for regions of stress concentration and necking. In these regions the mesh was refined to allow good simulation of necking and constraints caused by the notch. Models were meshed with three elements in the half thickness, 23 and 20 elements in the half width for models with radius 1 mm and 2 mm respectively. The element's dimension along the main loading direction is almost equal to its dimension along the width direction. Figure 2 shows the FE-discretisation of the centre regions of the U-notched specimens. Crack initiation and extension is modelled using the Gurson model. A crack has grown by the length of one element if the damage variable f^* reached the value of $0.99/q_1$. At this stage the stress carrying capacity is almost zero. For numerical reasons then the stiffness of the completely damaged element is set to a fraction of Young's modulus, i.e. $1/73000 E$.

4.2 Kahn Tear specimens

Shape and dimensions of the test specimens are shown in Figure 3. Specimens were machined in two directions with respect to the rolling direction of the sheet:

- along the rolling direction, L 'Longitudinal', three specimens,
- perpendicular to the rolling direction, T 'Transversal', three specimens,

For the FE-model of the specimen, one fourth of the specimen was modelled due to the twofold symmetry. The complete specimen was constructed with 3D quadratic solid elements with reduced integration. Figure 4 shows the respective quarter model. It should be mentioned that symmetry conditions can be exploited because the specimen's orientations are along the axes of orthotropy. Figure 5 shows the different levels of stress triaxiality appearing in the notched and Kahn specimens used in the investigations described here. Along the midplane ahead of the notch or crack tip the triaxiality exceeds the typical value of 0.66 for plane stress states.

During crack extension, energy is dissipated in the layer of elements in the process zone ahead of the crack tip. These elements comprise the layer located at the symmetry surface normal to the loading direction, see Figure 4. Energy is required to damage the elements until failure. This energy is proportional to the element dimension in the main loading direction. Therefore, the

mechanical behaviour outcome of the simulation is directly related to that dimension [42, 43]. Thus, the element dimension in the loading direction is considered as an additional parameter that is to be fitted to reproduce the experimental results. This characteristic dimension is usually correlated to the measured physical value of the mean nearest neighbour distance, d , of second phase precipitates in the alloy, which was determined to equal 14 μm for this material. The characteristic dimension (element height h) is fixed to 50 microns, which leads to a reasonable h/d -ratio of 3.6 [44] Four elements were used over the half thickness and 250 along the crack propagation direction (i.e. a size equal to 100 micron along the crack growth direction).

Experiments show that the crack initiates with a flat triangle and propagates in a slant mode of ductile tearing. It remains however difficult to match at the same time a slanted crack path and a correct load-displacement curve. Due to the difficulties encountered in modelling the transition, the crack is also modelled here as being flat, as in [28, 45].

5 RESULTS: UNIT CELL CALCULATIONS

5.1 Cell Models

Figure 6 reveals the overall stress response of the voided anisotropic RVEs. As expected, the maximum stress for each triaxiality depends on the orientation. The stress level of the L-orientation is highest, followed by that of the T-orientation. With D as the main loading direction, the stress level is significantly smaller. This is in line with the experimental findings and modelling results of macroscopic specimens [26]. More remarkable, however, is the difference in localisation or collapse strain between the orientations, indicated by the sudden drop of the effective stress. The L-orientation shows the smallest critical strain, increasing for the T- and D-orientations. This tendency holds for all triaxialities greater than 0.5. For mesoscopic stress states close to being uniaxial, localisation does not appear in a realistic range of strain: voids tend to elongate in the loading direction and contract in the transverse direction preventing the internal necking process from setting in. The well-known dependency of the fracture strain on the triaxiality [38] is reproduced by the RVE model in any case.

Another feature of the RVE models is shown in Figure 7: its ability to link the critical strain of void coalescence and the corresponding void volume fraction. The normalised void volume fraction is analysed as a function of the cell's equivalent strain. With increasing strain the void volume fraction evolves in an exponential manner. Once the critical strain of the cell is reached, an upturn in the void volume fraction is usually observed. In the present case this upturn is hardly visible. In order to identify the critical void volume fraction, the lateral strain, $-(E_y + E_z)$ is analysed as a function of the equivalent strain. Beyond the collapse point the lateral strain remains constant, whereas the effective strain and the void volume keep increasing. The collapse points identified for the different triaxialities and orientations are depicted in Figure 7 by solid circles. By comparing the three parts of Figure 7, it can be concluded that the orientation strongly affects the critical strain, E_c . For all triaxialities, E_c is larger in the D-orientation than in the T-orientation, which again is larger than in the L-orientation. However, the dependency of

the critical void volume fraction, f_c , on triaxiality for the different orientations, is less pronounced. Figure 8 summarises the relation derived from 3D RVE simulations, providing a micromechanical interpretation of the material's coalescence behaviour. For comparison, similar unit cell calculations based on axisymmetric structures obeying the same plastic hardening law, eqn. (1), have been performed and evaluated; the respective results are included in Figure 8. Although the mesoscopic ductility, E_c , is highest in the D-orientation, see Figure 6, the values for the critical void volume fraction are the smallest among the three orientations. This confirms that the anisotropy of the matrix affects the void growth rate. Void growth is retarded in the D-direction while plastic strain can easily accumulate. This effect is also visible for the T-orientation, leading to slightly smaller value of f_c compared to the L-orientation. This implies that for modelling the overall specimen behaviour, a direction-dependent f_c should be used. Beside this, Figure 8 shows the dependency of the critical porosity on triaxiality. The cell model results have been fitted by exponential functions as shown, providing that for all values of triaxialities the value of f_c is finite. This dependency has been incorporated in the continuum model, eqn. (A17). In detail, the following functions were obtained for L, T and D as the main loading direction:

$$\begin{aligned}
\text{L: } f_c &= f_0 \left(13.465 \exp \left[-\frac{T-0.422}{0.386} \right] + 19.0 \right) \\
\text{T: } f_c &= f_0 \left(13.465 \exp \left[-\frac{T-0.422}{0.386} \right] + 16.5 \right) \\
\text{D: } f_c &= f_0 \left(13.465 \exp \left[-\frac{T-0.422}{0.386} \right] + 14.5 \right)
\end{aligned} \tag{7}$$

It is assumed that when f has reached the critical value for the onset of coalescence $f_c(T)$, coalescence cannot be deactivated with f_c being fixed to the value reached when coalescence was first detected.

5.2 Parameter Calibration

In the Gurson model it is assumed that damage is governed by growth and coalescence of spherical voids. It is assumed in the following that the Gurson damage model including the definition of equivalent stress, eqn. (A12) gives the same mechanical response as the cell model explained earlier, provided that the initial void volume fraction, f_0 , is the same. It is worth mentioning that voids in Gurson model are assumed to grow isotropically even though the matrix material is anisotropic. In the cell model, the void's shape will evolve because of the direction-dependent plastic hardening. This effect cannot be captured by a damage model using only one scalar variable related to the void volume fraction.

The FE model of the homogenous solid cube representing the behaviour of the Gurson damage model is simple and consists of a single element loaded under constant triaxiality. In the cell model no void nucleation is considered. Consequently, void nucleation in Eq. (A16) is not used. Parameters q_1 and q_2 depend on the matrix material and have been calibrated so that the stress-

strain responses of the single element for different triaxialities match those of the cell model. Increasing either parameter will decrease the maximum stress and the reverse. The fit has been performed on the L-direction. Unlike the approach used in [45], the void evolution will be captured here by one numerical 'experiment' conducted in the L-direction only. For this orientation, the effect of q_2 is pronounced for higher triaxialities, while the effect of q_1 is almost identical for all triaxialities. The final calibrated values are $q_1=1.22$ and $q_2=1.16$. Figure 9 shows the cell model simulations for different triaxialities, and the corresponding fitted single element simulations.

Apparently, void growth becomes direction-dependent, but strain hardening has been calibrated from one test in the L-orientation only. Moreover, the parameters q_1 and q_2 of the continuum model do not depend on the direction either. Thus it might be conjectured that the model hardly can cope with the evolution of void volume fraction. In Figure 10 this has been proven not to be true. For two selected triaxialities, the void evolution predicted by the continuum model for the orientations in the T and D directions follows that of the cell model. In particular the growth rate is smaller for D loading. The modified GTN model can capture this trend as the ratio $\bar{\sigma}/R(p)$, see Eq. (A16), is smaller for this direction which is the softer one. Note that $\bar{\sigma}/R(p)$ is direction independent whereas the hydrostatic stress, σ_h , will depend on the loading direction for a given plastic strain level. From this it can be concluded that the implemented material law will predict the growth phase of initial voids realistically – at least from the viewpoint of micromechanics. It has to be noted that so far all parameters have been derived from uniaxial (mechanical) tests and analyses of RVEs. Further information, of course, can be obtained from mechanical tests aiming at the failure behaviour of the material.

6 RESULTS: SIMULATIONS OF TESTS

6.1 Fractography

The fracture surfaces of two Kahn specimens in the L- and T-directions were investigated by Scanning Electron Microscopy (SEM) to study their general geometrical characteristics, and to identify the failure mechanism. Subsequent to testing, several cross sections of the Kahn specimen loaded in the T-direction were investigated by SEM to confirm the failure mechanism and to study the region below the fracture surface.

Figure 11 shows that the crack initiates in a flat manner at the notch root (right in the picture). In both cases it turns later to a slanted fracture mode. In these specimens, two slanted surfaces are formed and the flat region between them has a shape of triangle. The slanted fracture surfaces make an angle of approximately 45 degrees with the loading direction as can be seen in the cross section, see Figure 12. Inspection of the entire set of tested Kahn specimens revealed that the fracture starts with a flat region – forced by the geometry of the notch – and then tilts at a certain point to form one or more slanted surfaces. The shape of the flat region, the transition from flat to slanted surface, the number and shape of slanted surfaces all vary from one specimen to

another. No special features could be found at the transition area from flat to slanted surface. While in the flat triangular zone ductile failure is predominant, along the slanted surfaces two mechanisms seem to be active: small regions of dimples and larger areas with transgranular separation along grain boundaries, which appear as flat surfaces.

Figure 13 reveals dimples being dominant on the fracture surface of the triangular zone. This structure results from ductile fracture by void growth and coalescence. Large dimples are present at the grain facets, while a larger number of smaller dimples are aligned at intergranular facets. The alloy Al 2198 is hardened by aging. In such alloys, the main source of voids is the disintegration between large inclusions with Fe and Si, dispersoids (Al_3Zr), fine hardening precipitates (Al_2CuLi , Al_3Li and Al_2Cu) and matrix material [46]. During loading, voids nucleate at these precipitates and grow, while new voids will be generated by further disintegration of precipitates from the matrix, and by breaking of precipitates. This can be seen from Figure 13 showing precipitates inside some dimples. Moreover, Figure 15 clearly shows the presence of voids at the tips of precipitates as well as broken precipitates originating voids. All this justifies the use of a porosity based model to address damage, at least for the description of crack initiation and the beginning of crack extension.

A mixed fracture mode consisting of transgranular and intergranular facets was observed in the slanted areas, see Figure 14 and Figure 16. The described mechanism might be complemented by a partially brittle behaviour. The fact that the surface always tilts and becomes slanted by approx. 45 degrees (the direction of maximum shear stress) supports this assumption. This partial brittleness explains the zig-zag shape of experimental (force vs. NOD) curves after load maximum, which is explained in the following section. It has to be mentioned here that it is questionable if the transition from a ductile damage mechanism to a transgranular failure can be described with a single continuum damage model.

6.2 U-notched specimens

The scatter between test results of each direction was negligible. Therefore, one specimen was chosen for each direction to represent the respective mechanical behaviour. Figure 17 displays the experimental results of the representative specimens in the three directions and the corresponding simulation results for notch radius 1 mm and 2 mm respectively. As already pointed out in [26], the maximum force of the specimen oriented in the T-direction is highest for notch radii of 1 mm and 2 mm, while the D-orientation shows a significantly lower force level. The direction-dependent force-elongation behaviour has been used in the past to calibrate the parameters in the anisotropic deformation model. By this means, the reverse of 'strength' order of the L- and T-directions between uniaxial tests (see table 2) and tests on notched specimens could be simulated [26]. In the present contribution special emphasis is put on the effect of damage evolution and realistic prediction of the ductility. Thus, the elongation at failure and the load decrease before final failure have to be exploited from the mechanical tests. The elongation at failure observed in the experiments is sorted in increasing order L, T, D for both notch geometries. While L and T-orientation differ only slightly, D shows a significantly higher failure

strain. This effect correlates well with the fracture surface appearance, where the amount of dimples is significantly higher on D-oriented specimens compared to those with L- or T-orientation revealing an increased ductility.

In order to capture this effect in the simulations, a void nucleation function was introduced with Eq. (A19). A constant nucleation intensity ($A=10$ for L-, T- and D-direction) was chosen here. In all cases it is assumed that independent of the initial porosity $f_0=0.0027$ being equal for all orientations, additional voids start to nucleate by particle fracture and/or debonding at a strain of $\varepsilon_0=0.4$. The high value chosen for the nucleation intensity is required to trigger the sharp drop of the load in simulations of the notched bar tests. The critical void volume fraction was defined to be triaxiality-dependent as explained in the previous paragraph, see Eq. (7). The acceleration factor for void coalescence was set to be equal 3. By this means, the damage and failure behaviour of the specimens with notch radius 2 mm has been successfully predicted, see Figure 17a. In the case of the sharp notch, Figure 17b, its higher triaxiality leads to a slight underestimation of the failure elongation. However, aiming at meeting the failure points of both geometries, the achieved result is acceptable. Interestingly, the sudden drop of the load in the simulations appears at different values of the total elongation for the L-, T- and D orientation, although the same nucleation function and the same damage parameters were used. The highest elongation is experimentally obtained for the D-direction, followed by the T-direction. This trend is reproduced in the simulations.

6.3 Kahn Tear Test

Figure 18 shows the behaviour of the six Kahn type specimens tested in terms of notch opening displacement, NOD, and applied force, F . Before reaching their respective load maximum, specimens oriented in the L-direction show a slightly higher load level compared to those oriented in the T-direction. This result is compatible with measurements performed by Morgeneyer [47] on Al-Cu-Mg alloy. At load maximum, after some crack extension, a transition to a more brittle failure behaviour can be seen. The crack extends rapidly leading to a significant stepwise decrease of the applied load. This behaviour is more pronounced for the L-oriented specimens. The T-oriented specimens show a more stable crack extension over the whole test range, leading to a higher toughness.

As the scatter between the test results of each orientation is negligible, one specimen was chosen for each direction to represent the respective mechanical behaviour. FE-simulations using the damage model were conducted to mimic the force-NOD behaviour. Figure 19 displays the experimental results of the two representative specimens and the corresponding simulation results. One can see from the simulation results that slight differences in a specimen's 'pre-fracture' deformation behaviour between the L- and T-orientation exist. Interestingly, the simulation predicts the opposite trend to that observed in the experiment: the T-orientation generally appears to be more fracture resistant than the L-orientation. In any case, the difference is small in the experimental data and hardly visible in Figure 19.

Furthermore, the simulations under predict the maximum force, but meet the decreasing part of the load-CMOD curve. This implies that the stable crack extension phase is not exactly met by the simulations, whereas the mixed-mechanism-phase is. This goes back to the calibration of the nucleation function used, Eq. (A19), which is based on the sudden load decrease obtained from the notched samples originating from a turn to a slanted failure mode. Consequently, the use of the strong nucleation rate aims rather at an assessment of the slanted failure mode instead of meeting the stable crack extension correctly.

For comparison, two simulations of the mechanical behaviour neglecting damage ($f=0$) are included in Figure 19. In this case, the trend of the T-direction's being stronger than the L-direction is also present, however less pronounced than in the simulations including damage evolution, indicating the presence of plastic anisotropy. The simulated curves follow the experimental ones closely up to the respective load maxima, which indicate that up to this point the macroscopic behaviour is primarily influenced by plastic deformation. For this kind of test the amount of stable crack extension is small.

7 CONCLUSIONS

These investigations provide new insight into two different fields of damage mechanics, namely the interaction of plastic anisotropy and evolution of void volume fraction on a general level and its application to the simulation of toughness anisotropy the fracture mechanisms of a commercial aluminium alloy in particular. The second part is complemented by a detailed investigation of the failure mechanisms obtained from fractography, revealing that two failure modes are present during crack extension.

In the first part, representative volume elements of a voided material are analysed under monotonous loading conditions in order to derive a micromechanically based criterion for void coalescence. It has been shown in a straight forward way that the evolution of a spherical void depends on the directionality of the surrounding material. This difference in void evolution influences the stage of beginning coalescence, which is direction-dependent and a function of the stress triaxiality. The method obviously has its limitations, as localisation in this type of unit cell does not appear for triaxialities less than 0.5 [15]. The obtained relationships for triaxiality, strain hardening and plastic anisotropy can be used to simulate the damage behaviour of an initially porous material on the basis of a modified Gurson-Tvergaard-Needleman constitutive model. Cell model simulations moreover help to fit Gurson parameters q_1 and q_2 in a systematic way. In this way, isotropic damage and plastic anisotropy are combined successfully.

Some remarks on the interaction between initial voids and a second population (of nucleated) voids in the unit cell simulations are justified here. The effect of strain controlled void nucleation on the failure strain (and hence on the porosity at coalescence) is nicely described e.g. in [48]. In the mentioned manuscript the authors state that the presence of a second

population of nucleated voids does not affect the growth of the first population of voids, but only their coalescence. In order to determine the critical volume fraction for this case, nucleation intensity and nucleation strain have to be known a priori. This is not the case in the current context, as the nucleation parameters have been determined from notched bars using the previously calibrated f_c -function considering primary voids only. Certainly the sequence matters here, and it depends on someone's preference whether the initial porosity and nucleation parameters are fixed first and the f_c -function is determined on this basis, or the nucleation function is added later.

Another controversial point might be the unit cell's aspect ratio. As pointed out before, assuming a cubic cell implies that voids are equally spaced in all three directions. In rolled sheets, however, an alignment of particles is often observed, which may lead to an easier coalescence in the direction perpendicular to the alignment direction. In the present case, the different ductilities of the material in the L-, T- and D-orientation could be predicted by assuming an isotropic void morphology. Consequently the particles's alignment does not play a role here.

Verification of the derived parameters was conducted by comparing simulation results to tests on notched tensile samples with two different notch radii, which differ with respect to the triaxiality exposed in the ligament. The different load evolutions in the three directions could be reproduced, but in order to meet the point of global failure a nucleation function at second-phase particle population had to be included in the model. This nucleation function was calibrated on the basis of these tests, and it turned out that the required nucleation rate starts at high values of plastic strain and contributes significantly to the overall failure. Although for all tested directions (L, T and D) the same set of model parameters (see Table 1) has been used, the differences in failure strain of notched samples could be predicted. This indicates that the void growth rate depends on the anisotropy of the matrix material. The lowest growth rate is here experienced in the D-orientation, the highest in the L-orientation.

Fracture tests on Kahn-specimens revealed two different fracture modes, which can be identified from the fracture surface as well as from the load-displacement record: a initial stage of ductile crack extension followed by a more pronounced ductile/brittle mode causing a sharp load drop. This load drop is more pronounced for specimens loaded in the L-direction (crack extension in the T-direction) than for those loaded in the T-direction (crack extension in the L-direction). This can be explained by the microstructure, because intergranular separation along elongated grains generally results in a higher toughness than separation perpendicular to the grain main axis. Simulations based on the void nucleation function are able to predict this behaviour and are thus suited for structural assessment. However, the load maximum will be well-predicted only if the nucleation function is not used, at the price of overestimating the toughness in the slanted failure regime.

8 ACKNOWLEDGEMENTS

This work has been carried out within the scope of the European Project COINS (Contract number AST5-CT 2006-030825). The present contribution was finalised during a sabbatical leave of D.S. at the Graduate Institute of Ferrous Technology (G.I.F.T.) of POSTECH, Pohang, Korea as part of an international outgoing fellowship (Marie Curie Actions) of the 7th programme of the European Commission. The authors acknowledge this support and hereby point out that the EU is not responsible for the content of this paper.

9 LITERATURE

- [1] Harris. Structural integrity of aging airplanes. In: Atluri SN, editor. International Symposium on Structural Integrity of Aging Airplanes. Atlanta: Springer; 1990. p. 141-152.
- [2] Nègre P, Steglich D, Brocks W. Crack extension in aluminium welds: a numerical approach using the Gurson-Tvergaard-Needleman model. *Eng Fract Mech.* 2004;71(16-17):2365-2383.
- [3] Roychowdhury S, Roy YDA, Dodds Jr. RH. Ductile tearing in thin aluminum panels: experiments and analyses using large-displacement, 3-D surface cohesive elements. *Eng Fract Mech.* 2002;69:983-1002.
- [4] Newman Jr. JC, James MA, Zerbst U. A review of the CTOA/CTOD fracture criterion. *Eng Fract Mech.* 2003;70:371-385.
- [5] Roy YDA, Dodds Jr. RH. Simulation of ductile crack growth in thin aluminum panels using 3-D surface cohesive elements. *Int J Fract.* 2001;110:21-45.
- [6] Lemaitre J. Local approach of fracture. *Eng Fract Mech.* 1986;25(5/6):523-527.
- [7] Pineau A. Development of the Local Approach to Fracture over the Past 25 years: Theory and Applications. *International Journal of Fracture.* 2006;138(1):139-166.
- [8] Doege E, El-Dsoki T, Seibert D. Prediction of necking and wrinkling in sheet-metal forming. *Journal of Materials Processing Technology.* 1995;50(1-4):197-206.
- [9] Chow CL, Yu LG, Tai WH, Demeri MY. Prediction of forming limit diagrams for AL6111-T4 under non-proportional loading. *International Journal of Mechanical Sciences.* 2001;43(2):471-486.
- [10] McClintock FA. A criterion for ductile fracture by the growth of holes. *J Appl Mech-Trans ASME.* 1968;363-371.
- [11] Rice JR, Tracey DM. On the ductile enlargement of voids in triaxial stress fields. *J Mech Phys Solids.* 1969;17:201-217.
- [12] Lee BJ, Mear ME. Axisymmetric deformation of power-law solids containing a dilute concentration of aligned spheroidal voids. *J Mech Phys Solids.* 1992;40(8):1805-1836.
- [13] Kalyanam S, Beaudoin AJ, Dodds Jr RH, Barlat F. Delamination cracking in advanced aluminum-lithium alloys - Experimental and computational studies. *Engineering Fracture Mechanics.* 2009;76(14):2174-2191.
- [14] Gologanu M, Leblond J-B, Devaux J. Approximate models for ductile metals containing non-spherical voids - case of axisymmetric prolate ellipsoidal cavities. *J Mech Phys Solids.* 1993;41(11):1723-1754.
- [15] Pardoën T, Hutchinson JW. An extended model for void growth and coalescence. *J Mech Phys Solids.* 2000;48(12):2467-2512.
- [16] Steglich D, Brocks W, Heerens J, Pardoën T. Anisotropic ductile fracture of Al 2024 alloys. *Engineering Fracture Mechanics.* 2008;75:3692-3706.

- [17] Ladeveze P. Towards a fracture theory. In: Owen DRJ, Onante E, Hinton E, editors. *Computational Plasticity: Fundamentals and Applications*. Barcelona; 1992. p. 1369-1400.
- [18] Krajcinovic D, Lemaitre J, Hult J, Murakami S, Sumarac D, Leckie FA, Najar J, editors. *Continuum Damage Mechanics - Theory and Applications*: Springer-Verlag; 1987.
- [19] Lemaitre J, Desmorat R, Sauzay M. Anisotropic damage law of evolution. *European Journal of Mechanics a-Solids*. 2000;19(2):187-208.
- [20] Hill R. A theory of the yielding and plastic flow of anisotropic metals. *Proc Roy Soc London A*. 1948;193:281-297.
- [21] Hill R. Constitutive modelling of orthotropic plasticity in sheet metals. *J Mech Phys Solids*. 1990;38:405-417.
- [22] Barlat F, Lian J. Plastic behavior and stretchability of sheet metals. Part I: A yield function for orthotropic sheets under plane stress conditions. *Int J Plast*. 1989;5(1):51-66.
- [23] Barlat F, Brem JC, Yoon JW, Chung K, Dick RE, Lege DJ, Pourboghraat F, Choi S-H, Chu E. Plane stress yield function for aluminum alloy sheets-part 1: theory. *Int J Plast*. 2003;19(9):1297-1319.
- [24] Benzerga AA, Besson J, Batisse R, Pineau A. Synergistic effects of plastic anisotropy and void coalescence on fracture mode in plane strain. *Modelling Simul Mater Sci Eng*. 2002;10:73-102.
- [25] Warner T. Recently-developed aluminium solutions for aerospace applications. *Materials Science Forum*. 2006;519-521:1271-1278.
- [26] Steglich D, Wafai H, Brocks W. Anisotropic Deformation and Damage in Aluminium 2198 T8 Sheets. *Int J Damage Mechanics*. 2009.
- [27] Bron F, Besson J. A yield function for anisotropic materials: Application to aluminium alloys. *Int J Plast*. 2004;20(4-5):937-963.
- [28] Bron F, Besson J. Simulation of the ductile tearing for two grades of 2024 aluminum alloy thin sheets. *Eng Fract Mech*. 2006;73(11):1531-1552.
- [29] Rousselier G. Ductile fracture models and their potential in local approach of fracture. *Nucl Eng Des*. 1987;105:97-111.
- [30] Besson J, Foerch R. Large scale object-oriented finite element code design. *Computer Methods in Applied Mechanics and Engineering*. 1997;142(1-2):165-187.
- [31] Koplik J, Needleman A. Void growth and coalescence in porous plastic solids. *Int J Solids Struct*. 1988;24(8):835-853.
- [32] Brocks W, Hönl A, Sun D-Z. Verification of the transferability of micromechanical parameters by cell model calculations with visco-plastic materials. *Int J Plast*. 1995;11(8):971-998.
- [33] Hom CL, McMeeking RM. Void growth in elastic plastic materials. *J Appl Mech-Trans ASME*. 1989;56:309-317.
- [34] Kuna M, Sun DZ. Three-dimensional cell model analyses of void growth in ductile materials. *Int J Fract*. 1996;81:235-258.
- [35] Worswick MJ, Pick RJ. Void growth and constitutive softening in a periodically voided solid. *J Mech Phys Solids*. 1990;38(5):601-625.
- [36] Yerra SK, Tekoglu C, Scheyvaerts F, Delannay L, Van Houtte P, Pardoën T. Void growth and coalescence in single crystals. *International Journal of Solids and Structures*. 2010;47(7-8):1016-1029.
- [37] Steglich D, Wafai H, Brocks W. Anisotropic Deformation and Damage in Aluminium 2198 T8 Sheets. *Int J Damage Mechanics*. 2010;19(2):131-152.
- [38] Kim J, Gao X, Srivatsan TS. Modeling of void growth in ductile solids: effects of stress triaxiality and initial porosity. *Eng Fract Mech*. 2004;71:379-400.
- [39] Zhang KS, Bai JB, François D. Numerical analysis of the influence of the Lode parameter on void growth. *Int J Solids Struct*. 2001;38:5847-5856.

- [40] Kahn NA, Imbembo EA. A method of evaluating transition from shear to cleavage failure in ship plate and its correlation with large-scale plate tests. *Welding J.* 1948;27(4):169-184.
- [41] Sun D-Z, Hömig A, Böhme W, Schmitt W. Application of micromechanical models to the analysis of ductile fracture under dynamic loading. In: Erdogan F, Hartranft RJ, editors. *Fracture Mechanics*, 25th Vol: American Society for Testing and Materials; 1994. p. 343-357.
- [42] Besson J, Steglich D, Brocks W. Modeling of plane strain ductile rupture. *Int J Plast.* 2003;19:1517-1541.
- [43] Ruggieri C, Panontin TL, Dodds Jr. RH. Numerical modeling of ductile crack growth in 3-D using computational cell elements. *Int J Fract.* 1996;82:67-95.
- [44] Steglich D, Brocks W. Micromechanical modelling of damage and fracture of ductile materials. *Fatigue Fract Eng Mater Struct.* 1998;21:1175-1188.
- [45] Morgeneyer TF, Besson J, Proudhou H, Starink MJ, Sinclair I. Experimental and numerical analysis of toughness anisotropy in AA2139 Al-alloy sheet. *Acta Materialia.* 2009;57(13):3902-3915.
- [46] Robson JD, Prangnell PB. Dispersoid precipitation and process modelling in zirconium containing commercial aluminium alloys. *Acta Materialia.* 2001;49(4):599-613.
- [47] Morgeneyer TF, Starink MJ, Sinclair I. Evolution of voids during ductile crack propagation in an aluminium alloy sheet toughness test studied by synchrotron radiation computed tomography. *Acta Materialia.* 2008;56(8):1671-1679.
- [48] Fabregue D, Pardoën, T. A constitutive model for elastoplastic solids containing primary and secondary voids. *Journal of the Mechanics and Physics of Solids.* 2008;56:719-741.
- [49] Karafillis AP, Boyce MC. A general anisotropic yield criterion using bounds and a transformation weighting tensor. *Journal of the Mechanics and Physics of Solids.* 1993;41(12):1859-1886.
- [50] Barlat F, Lege DJ, Brem JC. A six-component yield function for anisotropic materials. *International Journal of Plasticity.* 1991;7(7):693-712.
- [51] Gurson AL. Continuum theory of ductile rupture by void nucleation and growth: part I - yield criteria and flow rules for porous ductile media. *J Eng Mater Technol-Trans ASME.* 1977;99:2-15.
- [52] Tvergaard V, Needleman A. Analysis of the cup-cone fracture in a round tensile bar. *Acta Metall.* 1984;32(1):157-169.

APPENDIX

The anisotropic plastic potential used in this work is based on a yield surface according to Bron and Besson [27] incorporating the effect of hydrostatic pressure on the growth of micro-voids. Hardening and damage evolution are assumed as isotropic. With regard to the description of anisotropic yielding, a Voigt notation is used for all tensors in the following. The second order symmetric stress tensor is represented by a six-component vector,

$$\begin{aligned}\underline{\sigma}^T &= (\sigma_i) = (\sigma_1 \quad \sigma_2 \quad \sigma_3 \quad \sigma_4 \quad \sigma_5 \quad \sigma_6) \\ &= (\sigma_{11} \quad \sigma_{22} \quad \sigma_{33} \quad \sqrt{2}\sigma_{12} \quad \sqrt{2}\sigma_{23} \quad \sqrt{2}\sigma_{31})\end{aligned}\quad (A8)$$

As in the classical theory of incremental, rate-independent plasticity, yielding is modelled by a convex yield surface, which encloses all stress states causing elastic deformations and expands isotropically during plastic deformation. The yield condition is written as

$$\varphi(\underline{\sigma}, \underline{\varepsilon}^p) = \bar{\sigma} - R(p) = 0, \quad (\text{A9})$$

where $\bar{\sigma}$ is an appropriately defined equivalent stress, $R(p)$ the current flow stress, and p the associated accumulated equivalent plastic strain. As the hydrostatic stress, i.e. the first invariant of the stress tensor,

$$\sigma_h = \frac{1}{3} \sum_{k=1}^3 \sigma_k, \quad (\text{A10})$$

does not affect plastic yielding, the yield surface is described by the deviatoric stresses

$$\sigma'_i = \begin{cases} \sigma_i - \sigma_h & i = 1, 2, 3 \\ \sigma_i & i = 4, 5, 6 \end{cases}. \quad (\text{A11})$$

Isotropic behaviour requires that the equivalent stress, $\bar{\sigma}$, depends on the stress invariants, only.

Bron and Besson [27] defined an equivalent stress

$$\bar{\sigma} = \left[\alpha \bar{\sigma}_1^a + (1 - \alpha) \bar{\sigma}_2^a \right]^{1/a}, \quad (\text{A12})$$

by the superposition of two functions

$$\begin{aligned} \bar{\sigma}_1 &= \left[\frac{1}{2} \left[\left| s_I^{(1)} - s_{II}^{(1)} \right|^{b_1} + \left| s_{II}^{(1)} - s_{III}^{(1)} \right|^{b_1} + \left| s_{III}^{(1)} - s_I^{(1)} \right|^{b_1} \right] \right]^{1/b_1}, \\ \bar{\sigma}_2 &= \left[\frac{3^{b_2}}{2^{b_2} + 2} \left(\left| s_I^{(2)} \right|^{b_2} + \left| s_{II}^{(2)} \right|^{b_2} + \left| s_{III}^{(2)} \right|^{b_2} \right) \right]^{1/b_2}, \end{aligned} \quad (\text{A13})$$

where $s_I^{(k)}$, $s_{II}^{(k)}$, $s_{III}^{(k)}$ ($k = 1, 2$) are the principal values of two modified stress deviators defined as

$$\underline{s}^{(k)} = \underline{\underline{L}}^{(k)} \cdot \underline{\sigma}^{(k)}, \quad (\text{A14})$$

with

$$\underline{\underline{\mathbf{L}}}^{(k)} = (\underline{\underline{L}}_{ij}^{(k)}) = \begin{pmatrix} (c_2^{(k)} + c_3^{(k)})/3 & -c_3^{(k)}/3 & -c_2^{(k)}/3 & 0 & 0 & 0 \\ -c_3^{(k)}/3 & (c_3^{(k)} + c_1^{(k)})/3 & -c_1^{(k)}/3 & 0 & 0 & 0 \\ -c_2^{(k)}/3 & -c_1^{(k)}/3 & (c_1^{(k)} + c_2^{(k)})/3 & 0 & 0 & 0 \\ 0 & 0 & 0 & c_4^{(k)} & 0 & 0 \\ 0 & 0 & 0 & 0 & c_5^{(k)} & 0 \\ 0 & 0 & 0 & 0 & 0 & c_6^{(k)} \end{pmatrix}. \quad (\text{A15})$$

The four material parameters a , b_1 , b_2 , α , affect the shape of the yield surface, but not its anisotropy, which is controlled by the 12 constants $c_i^{(k)}$, $k = 1, 2$, $i = 1, \dots, 6$. Altogether, the yield function contains 16 parameters. To ensure convexity and differentiability, $a \geq 1$ and $b_k \geq 2$ is required as Bron and Besson [27] showed. In the case of $c_i^{(1)} = c_i^{(2)}$ and $a = b_1 = b_2$, Bron's yield function corresponds to that of Karafillis and Boyce [49], and for $\alpha = 1$ to the yield function of Barlat et al. [50]. The yield function of von Mises, Eq. (6), is obtained for $\alpha = 1$ and $c_i = 1$ if $a = 2$ or 4, and that of Tresca if $a = 1$ or $+\infty$.

Damage of the material results in softening and requires the incorporation of the hydrostatic stress into the yield function. The most common model for isotropic damage in ductile materials is the GTN model named after Gurson [51], Tvergaard and Needleman [52], who proposed a yield surface described by

$$\frac{\bar{\sigma}^2}{R^2(p)} + 2q_1 f^* \cosh\left(q_2 \frac{3\sigma_h}{2R(p)}\right) - 1 - (q_1 f^*)^2 = 0. \quad (\text{A16})$$

f^* is a scalar internal variable of damage related to the void volume fraction or porosity, f , and q_1 , q_2 are additional model parameters. Here, the von Mises stress has been replaced by the effective stress as in [28]. To account for void coalescence, damage is accelerated by using a stepwise linear function of the void volume fraction,

$$f^* = \begin{cases} f & \text{for } f < f_c(T) \\ f_c + K(f - f_c(T)) & \text{for } f \geq f_c(T) \end{cases}. \quad (\text{A17})$$

The porosity develops by two contributions, namely by void nucleation and void growth,

$$\dot{f} = \dot{f}_{nuc} + \dot{f}_{growth}. \quad (\text{A18})$$

For the nucleation term different functions have been proposed. Following the popular assumption to link nucleation rate to plastic equivalent strain, a constant nucleation rate starting at a threshold value of the plastic equivalent strain is used in the present contribution,

$$\dot{f}_{nuc} = A H(p - \varepsilon_0), \quad (\text{A19})$$

with H being the Heaviside function and A and ε_0 model parameters. This was chosen to support void nucleation at high plastic strains on a phenomenological basis.

Void growth evolves following

$$\dot{f}_{growth} = (1 - f) \sum_{k=1}^3 \dot{\varepsilon}_{kk}^p = (1 - f) \dot{\varepsilon}_{vol}^p, \quad (\text{A20})$$

starting with an initial porosity f_0 .

Table 1: Model parameters used in the simulations

Parameter	Value	Parameter	Value
E [MPa]	73000	ν	0.3
α	0.5	b_1	16
a	16	b_2	16
$c_1^{(1)}$	1.010	$c_1^{(2)}$	1.128
$c_2^{(1)}$	1.073	$c_2^{(2)}$	0.810
$c_3^{(1)}$	1.005	$c_3^{(2)}$	0.945
$c_4^{(1)}$	1.243	$c_4^{(2)}$	1.003
$c_5^{(1)}$	1.000	$c_5^{(2)}$	1.000
$c_6^{(1)}$	1.000	$c_6^{(2)}$	1.000
f_0	0.0027	-	-
ε_0	0.4	$A_L/A_T/A_D$	10/10/10
f_c	$f_c(T)$	K	3
q_1	1.22	q_2	1.16

Table 2: Measured mechanical properties of Al 2198 T8

Tensile direction	Yield stress [MPa]	Tensile strength [MPa]	R-value [.]	Fracture strain [.]
L	469	510	0.7	0.14
T	452	498	1.5	0.13
D	394	436	2.0	0.16

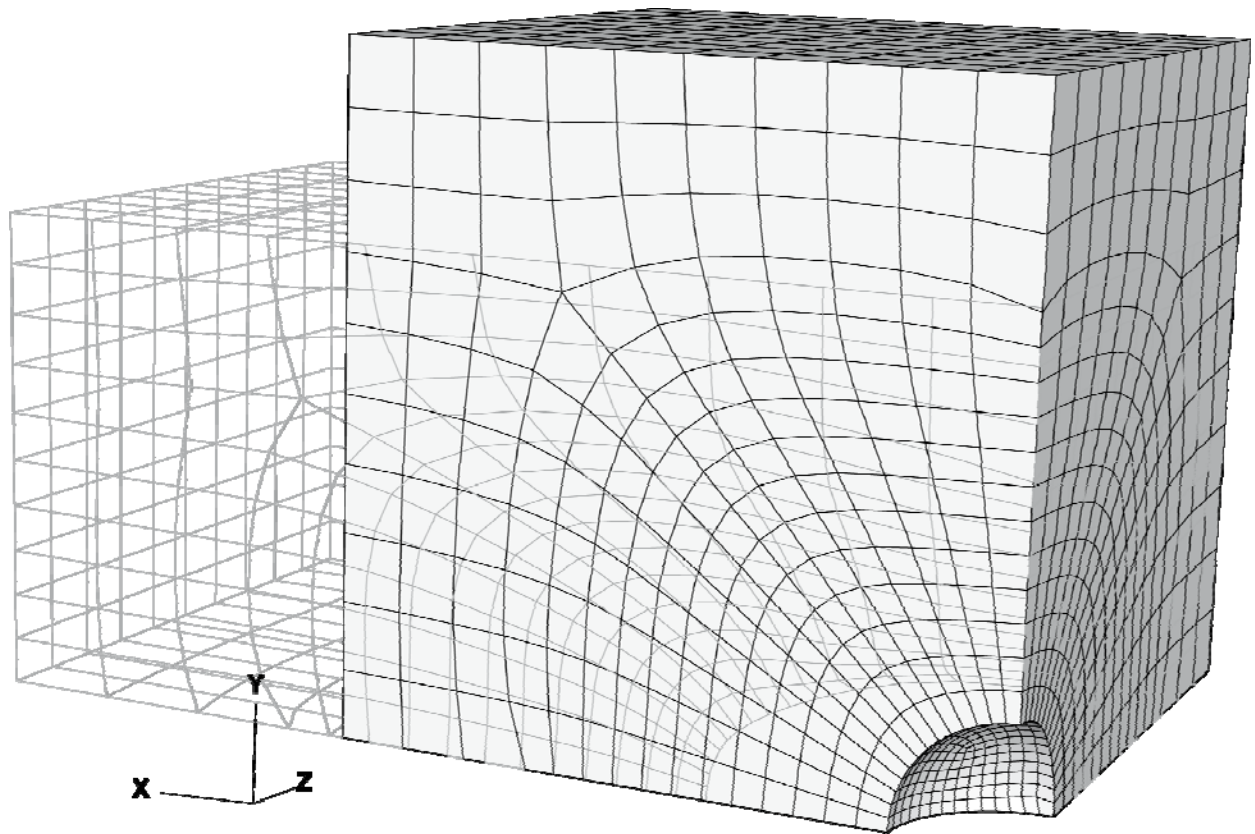


Figure 1: FE-model of a primitive cubic unit cell (1/8 model): initial and deformed configuration; the applied triaxiality is 0.5

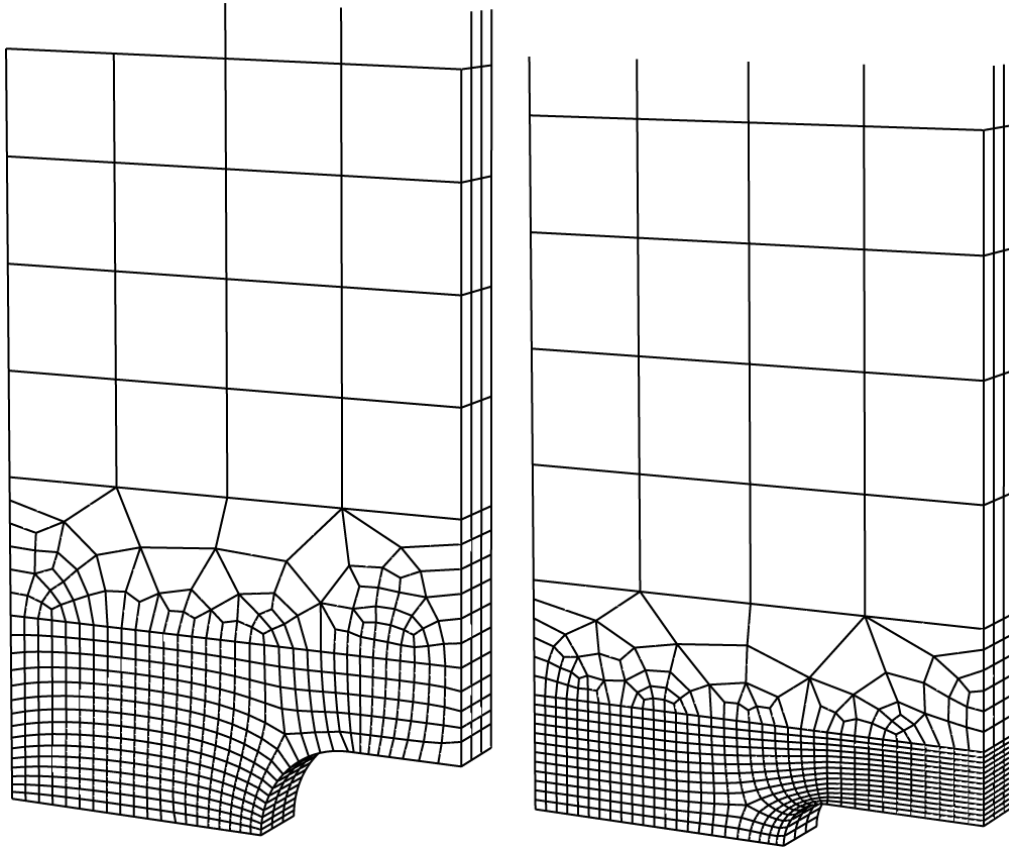


Figure 2: 3D FE discretisations of the U-notched specimens ($r=2$ mm, $r=1$ mm) using full symmetry

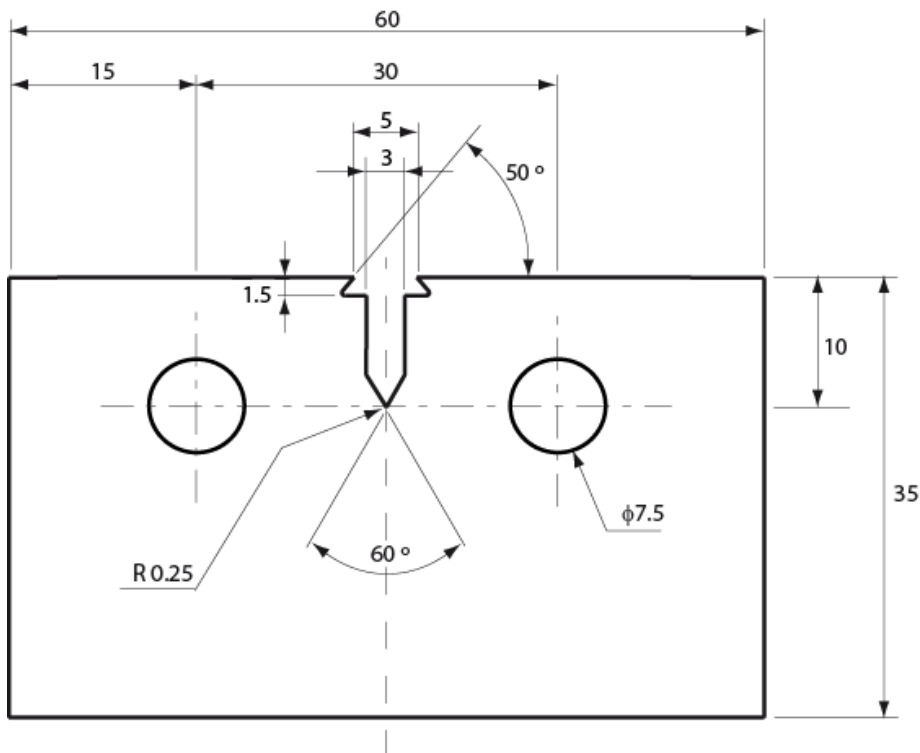


Figure 3: Sketch of the Kahn specimen used in the present investigation (dimensions in mm)

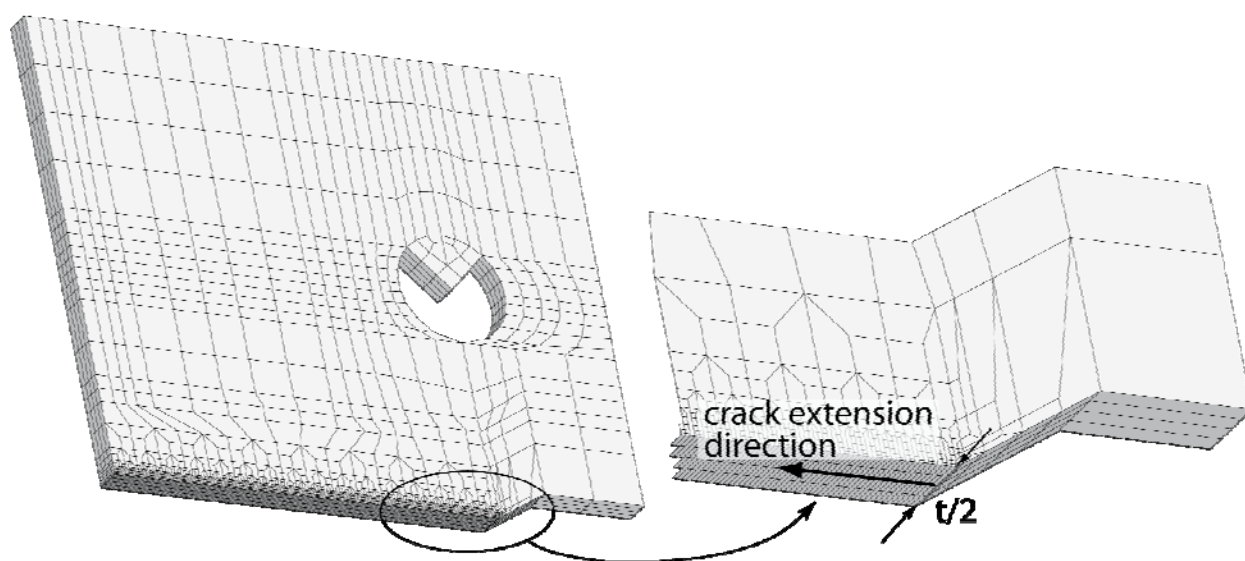


Figure 4: FE-mesh of a Kahn specimen, magnification of the initial crack tip region

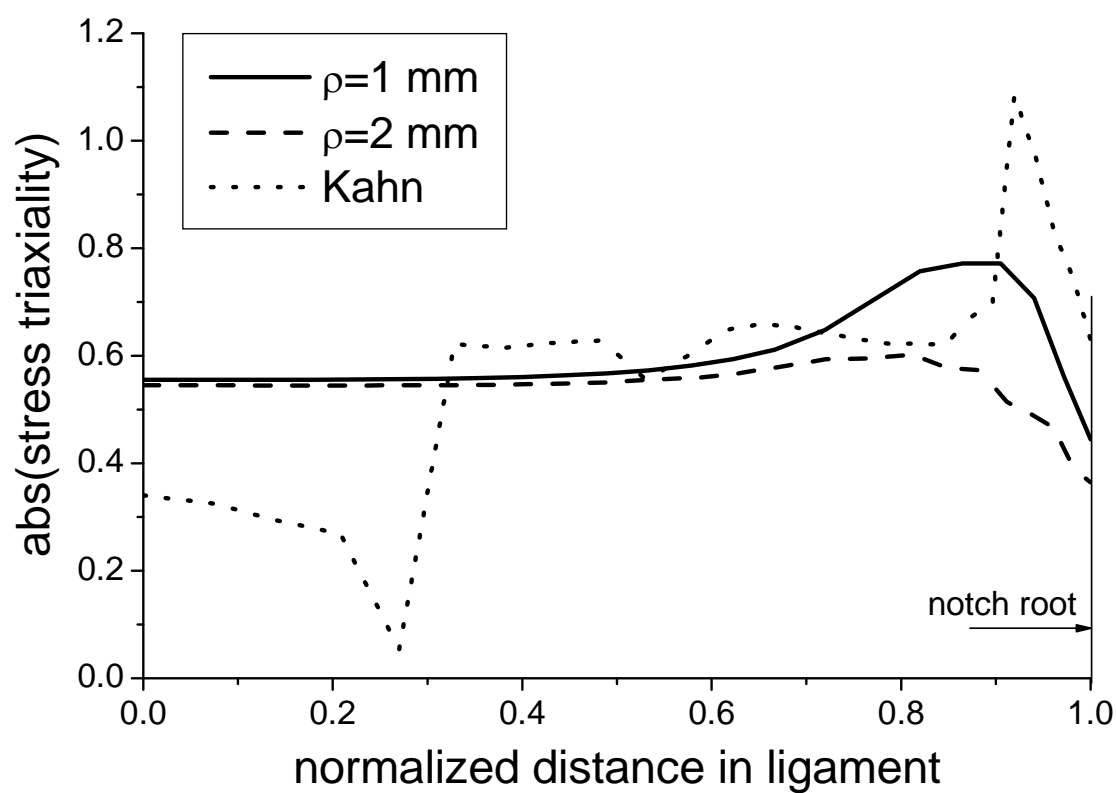


Figure 5: Stress triaxiality in the midplane of the three investigated specimens at maximum load

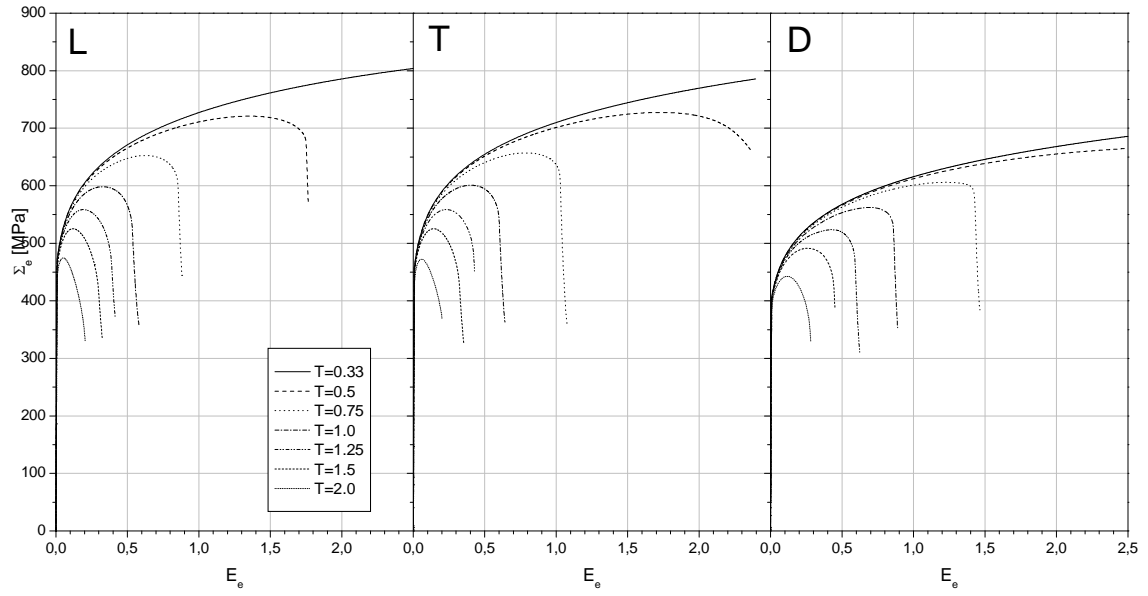


Figure 6: Mechanical responses of the unit cells for different orientations and triaxialities in terms of mesoscopic stresses and strains

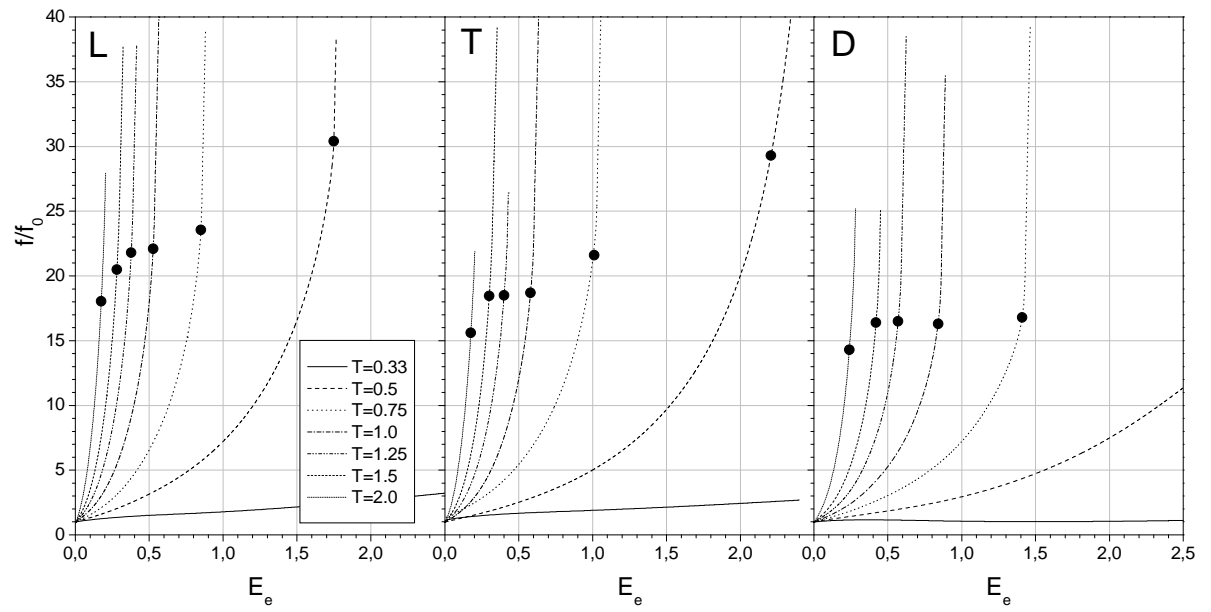


Figure 7: Mechanical response of the unit cells for different orientations and triaxialities in terms of void evolution as a function of equivalent macroscopic strain. Circles indicate states of void coalescence

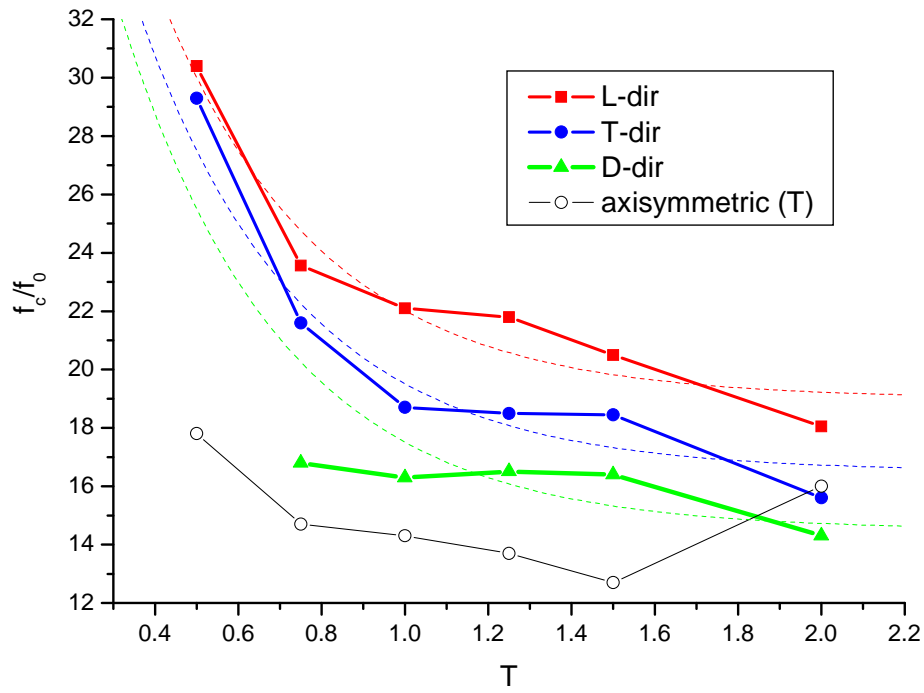


Figure 8: Dependency of critical void volume fraction on triaxiality and material orientation derived from 3D simulations. Axisymmetric model is shown for comparison ($f_0=0.0027$). Dashed lines represent the fitting functions.

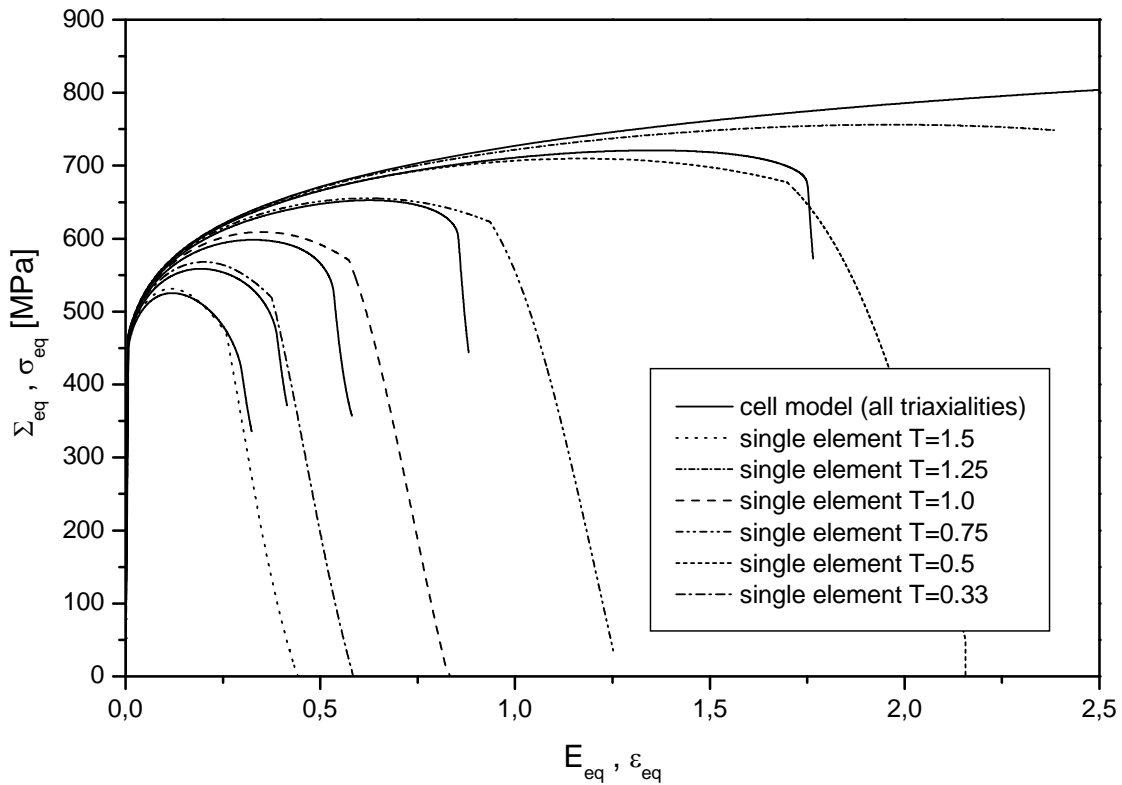


Figure 9: Determination of the Gurson parameters by reconciling with cell model predictions

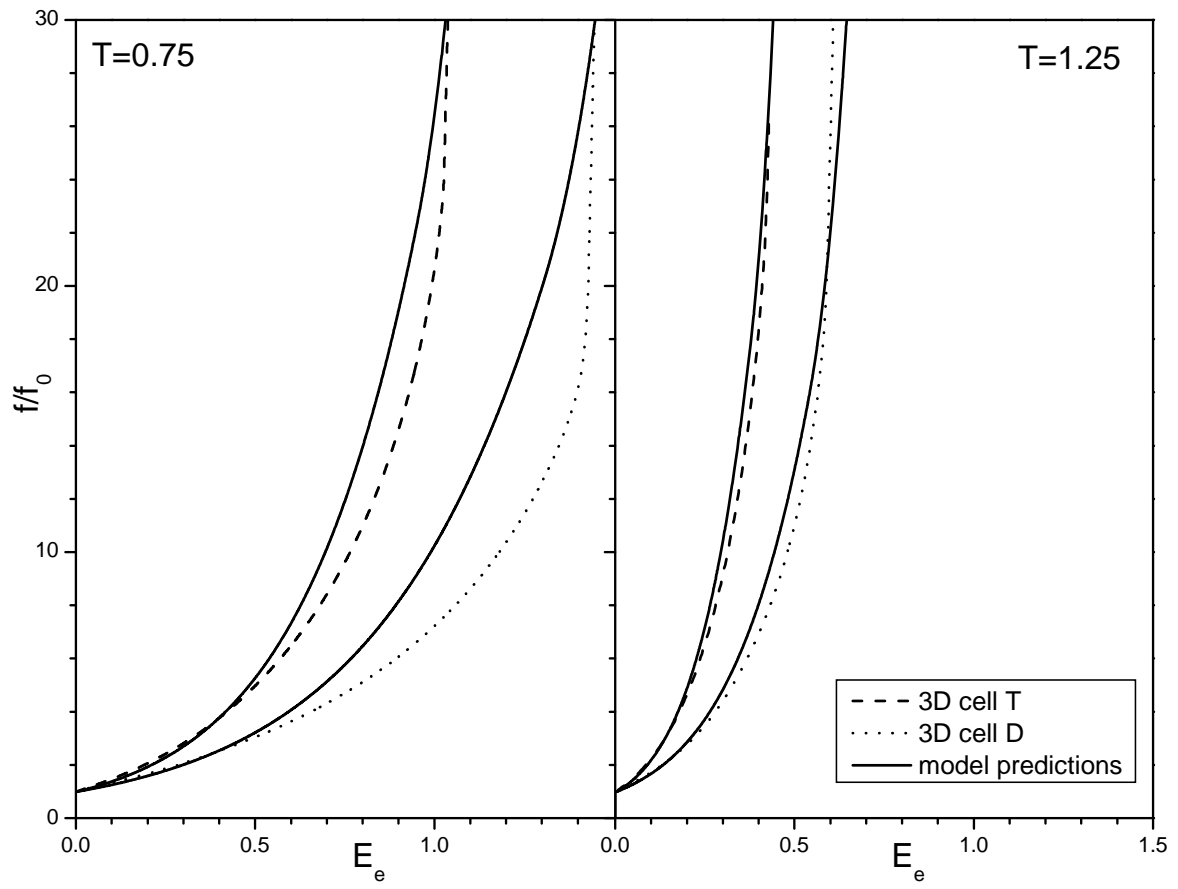


Figure 10: Void evolution in the case of T and D being main loading directions for cell and continuum model for two values of triaxiality

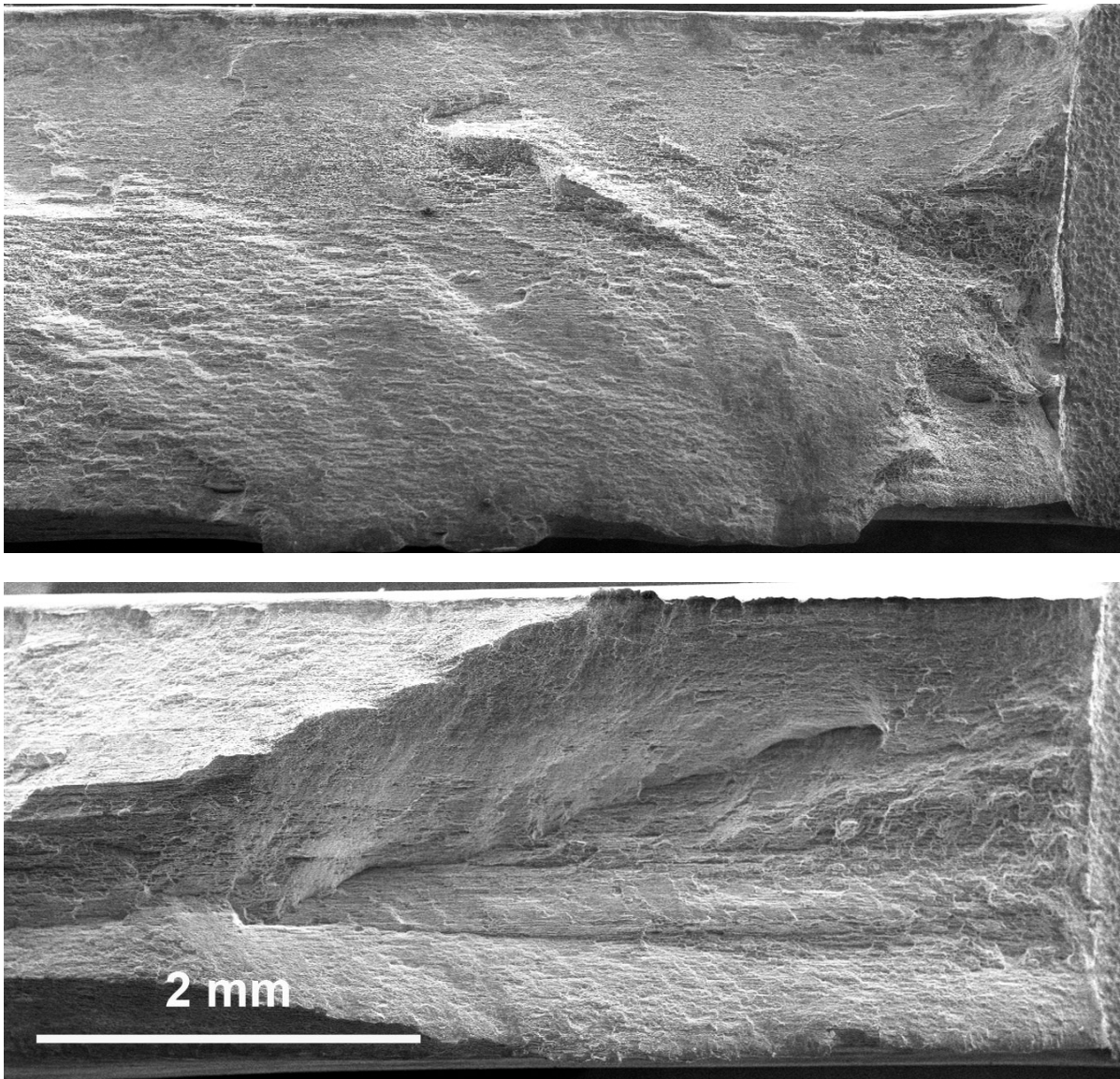


Figure 11: Global view of a Kahn specimen fracture surface (top: L main loading direction, bottom: T main loading direction) showing crack initiation and extension, flat and slanted regions

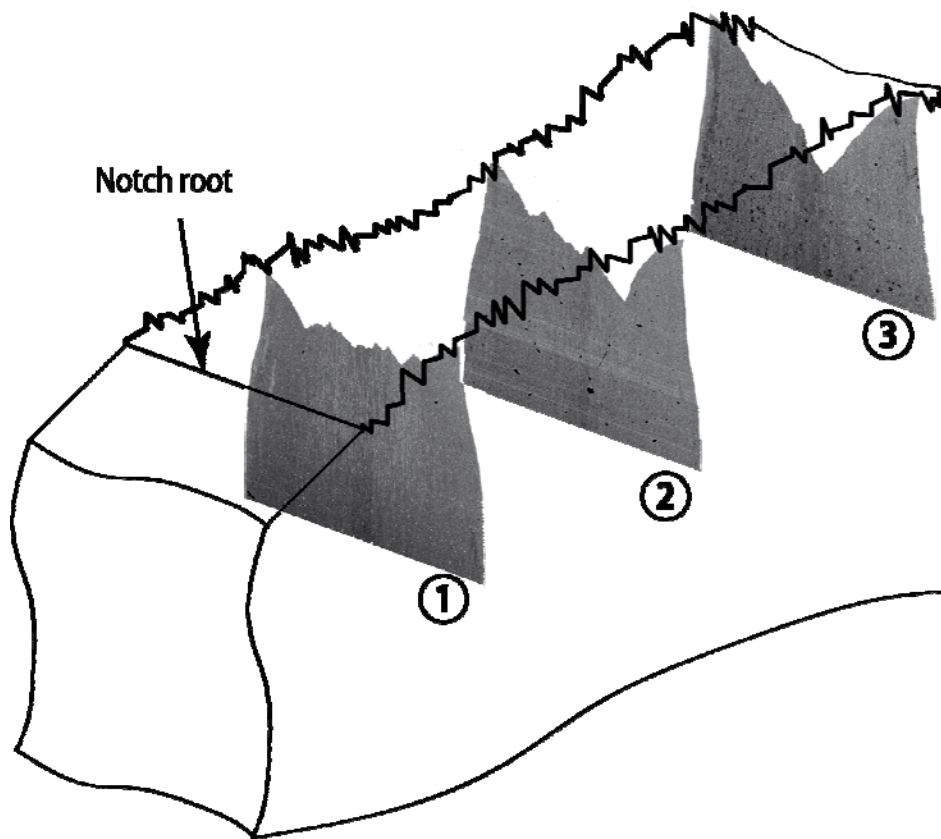


Figure 12: Overview of serial sectioning of Kahn specimen's ligament (T main loading direction)

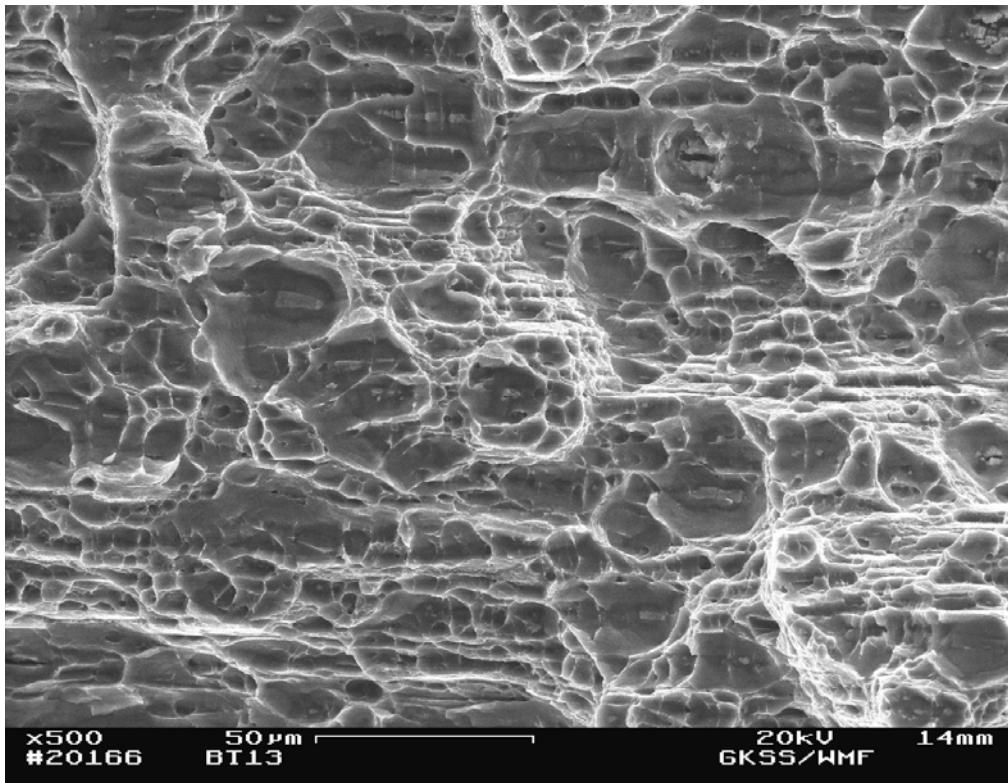


Figure 13: Fractograph showing the triangular zone of crack transition in a Kahn specimen (T main loading direction) with its dominant dimple structure

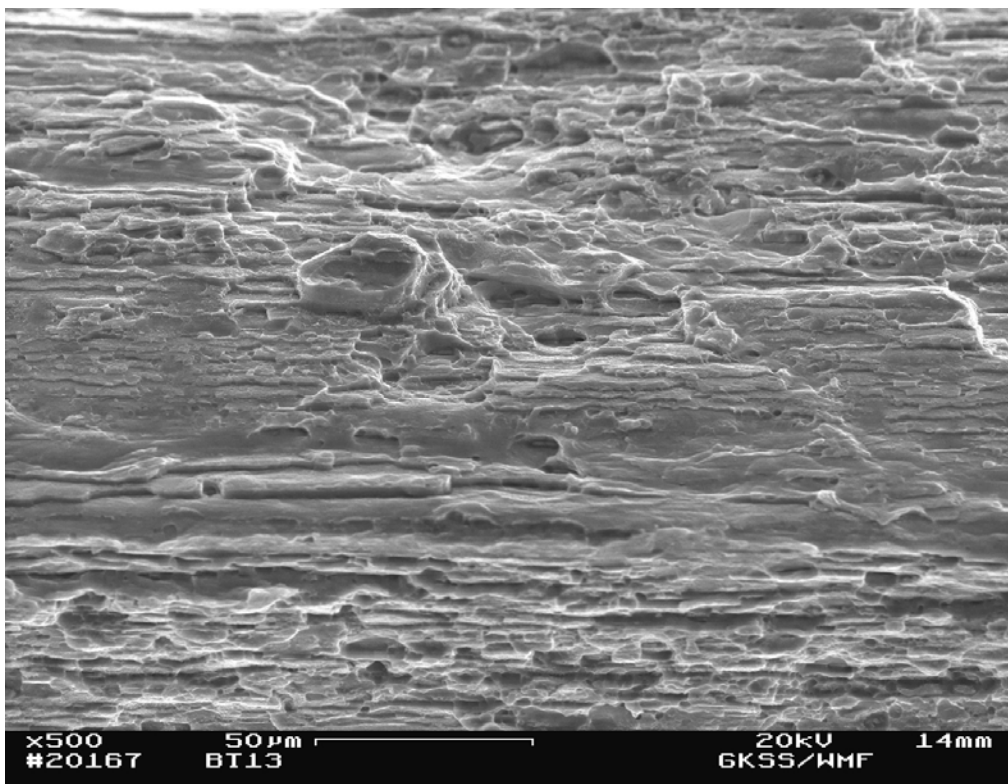


Figure 14: Fracture surface of a Kahn specimen taken from the slanted region showing a dimple structure and transgranular debonding along grain boundaries (T main loading direction)

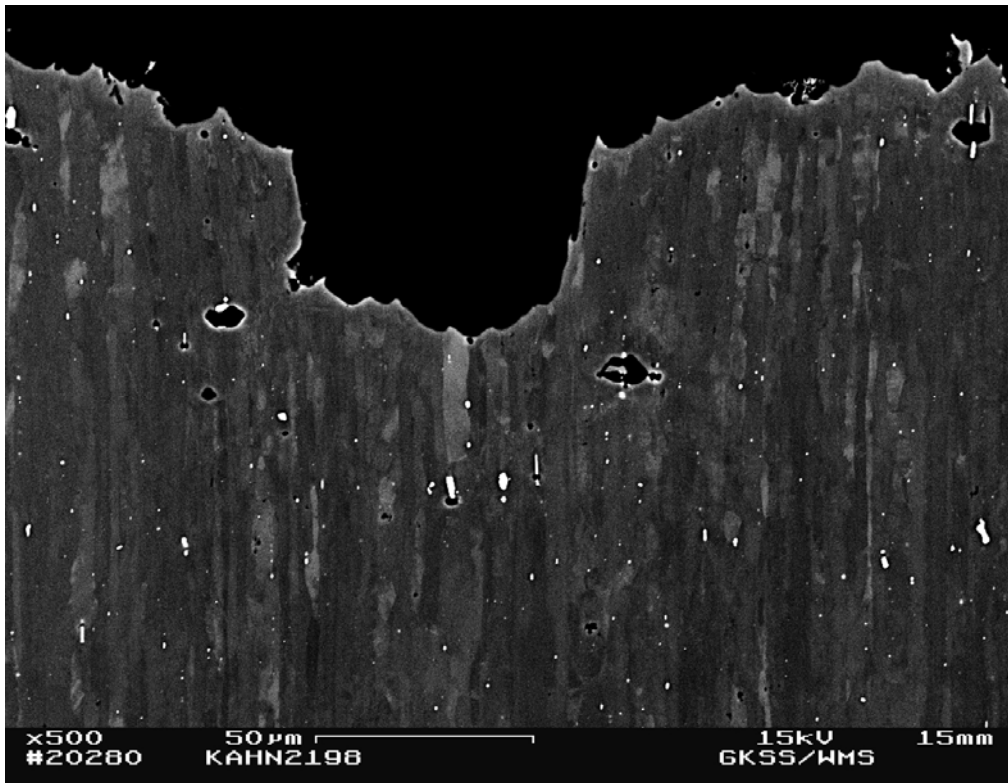


Figure 15: Region below the fracture surface (section 1, zone of flat separation, see Figure 12) showing a high number of voids (black) and partly broken precipitates (white)

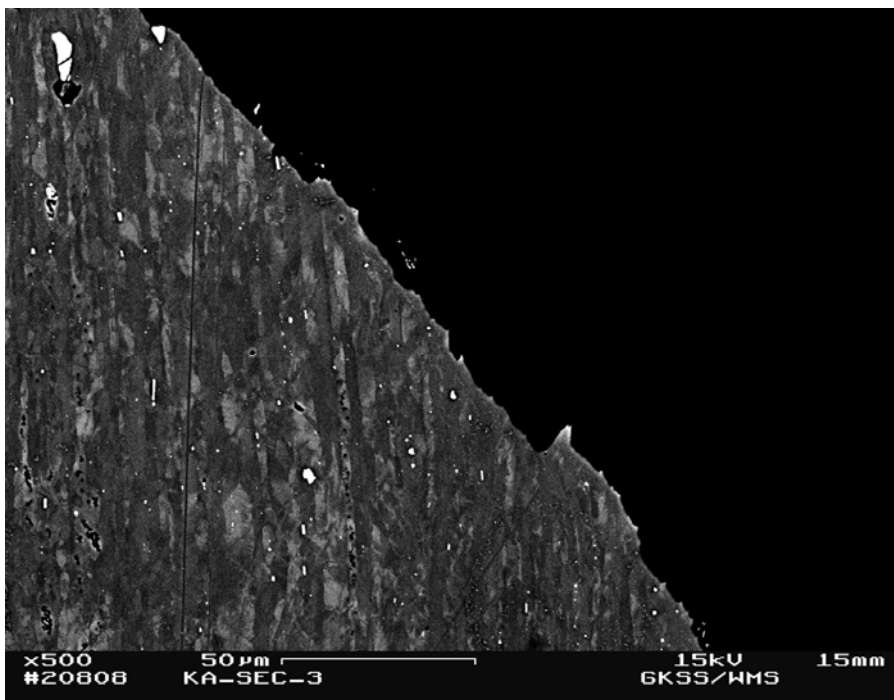


Figure 16: Region below the fracture surface at the slanted crack front (section 3, see Figure 12) showing less features of ductile failure

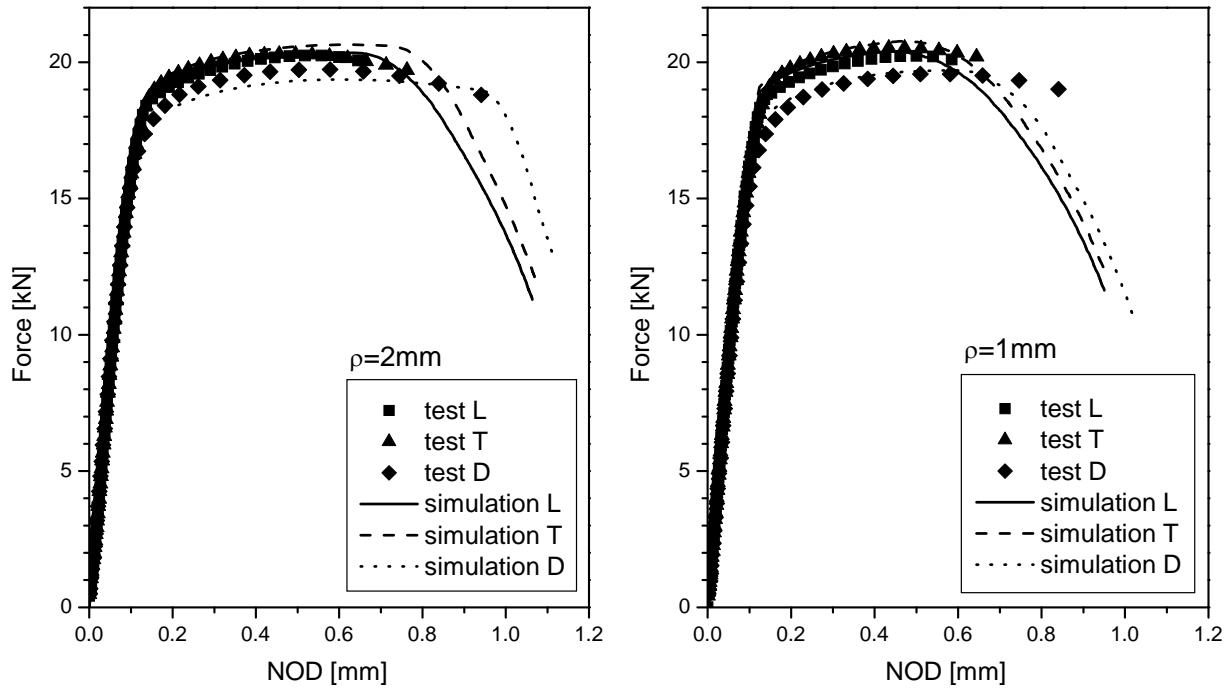


Figure 17: Response of the U-notched samples $\rho=2\text{ mm}$ (a) and $\rho=1\text{ mm}$ (b) – experiment and simulation using the damage model

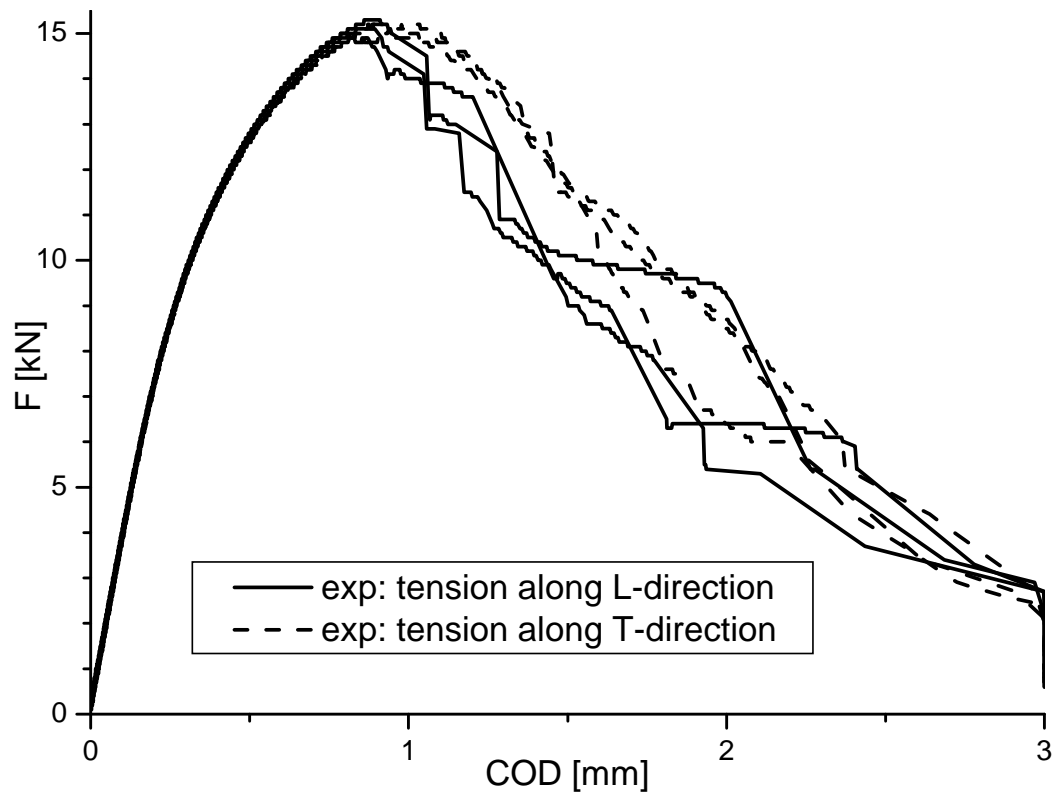


Figure 18: Results of the Kahn tear tests for specimens loaded in L- and T-orientation

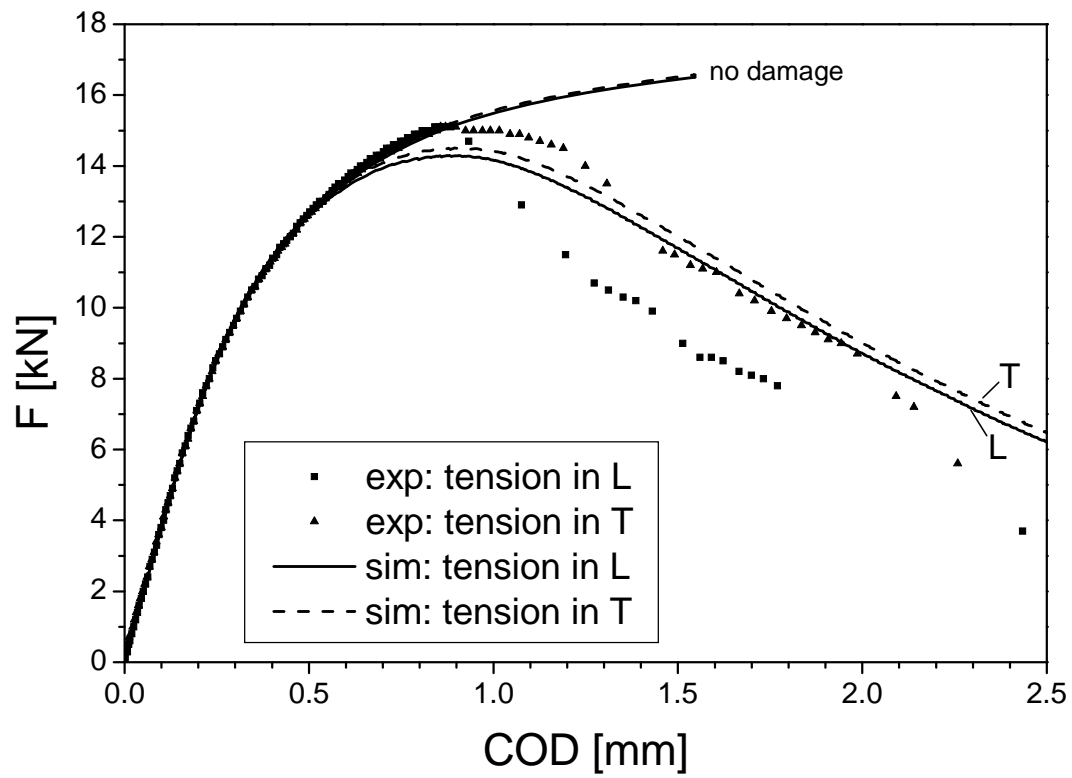


Figure 19: Results of the FE-simulations of the Kahn tear tests in comparison with experimental data